INL/EXT-19-55645

Revision 0

Post-Irradiation Examination of the ATF-1 Experiments – 2019 Status

Fabiola Cappia
Jason M. Harp

September 2019

The INL is a U.S. Department of Energy National Laboratory
operated by Battelle Energy Alliance

INL/EXT-19-55645
Revision 0

Post-Irradiation Examination of the ATF-1 Experiments – 2019 Status

Fabiola Cappia
Jason M. Harp

September 2019

Idaho National Laboratory
Idaho Falls, Idaho 83415

http://www.inl.gov

Prepared for the
U.S. Department of Energy
Office of Nuclear Energy
Under DOE Idaho Operations Office
Contract DE-AC07-05ID14517

INTENTIONALLY BLANK

SUMMARY

A collaborative effort of the Advanced Fuels Campaign together with industry consortia is focused on the development of enhanced Accident Tolerant Fuels (ATF) for Light Water Reactors (LWRs). The scoping studies, referred to as ATF-1 irradiations, are being performed in the Advanced Test Reactor of Idaho National Laboratory using drop-in style irradiations. The Post-Irradiation Examinations (PIEs) of ATF-1 began in 2017 and continued in 2019. This report describes the results of examinations on ATF-1 irradiations designed to test the performance of advanced iron-based cladding, including compatibility of FeCrAl with UO_2, and ATF-1 irradiation of U_3Si_5.

Two rodlets with commercial iron-based cladding and UO_2 pellets have been irradiated to low burnup (i.e., < 20 GWd/tHM). The first rodlet had an Alloy33® cladding, while the other had a Kanthal APMT® cladding. The performed PIEs were focused on the determination of fuel microstructure, evaluation of fuel-cladding interaction and irradiation-induced variations of cladding mechanical properties. For both rodlets, no significant changes in the cladding hardness were measured, and the cladding hoop strain remained limited. Gamma tomography revealed no Cs axial migration as expected for LWR fuel, but significant cesium radial migration, which was induced by thermal migration consequent to high irradiation temperatures compared to standard LWR irradiation temperatures. Microstructure analyses revealed formation of secondary phases along the pellet rim of samples from both rodlets. No wastage or extensive chemical interaction between the fuel and the internal wall of the cladding was observed, suggesting that the secondary phases accumulated at the pellet rim might be due to formation of Cs-U-O compounds. However, further advanced PIEs are necessary to confirm this hypothesis.

Optical microscopy analysis of the rodlet designed by Oak Ridge National Laboratory to evaluate the interaction between UO_2 and various FeCrAl alloys revealed no extensive interaction in all the samples irradiated in the rodlet. Localized defects, namely circular pitting and cracks of a few tens of microns, were observed on the FeCrAl disc surfaces in some of the diffusion couples. These defects might be surface fabrication defects rather than irradiation-induced localized corrosion, but chemical analyses are needed to determine whether accumulation of corrosive fission products are causing enhanced interaction.

Both non-destructive and destructive PIEs were collected on a rodlet containing U_3Si_5 fuel, irradiated at 13.19 GWd/tHM. The rodlet had extremely low fission gas release, similar to previously analyzed U_3Si_2 rodlets. Gamma tomography revealed thermo-migration of fission product ruthenium toward the center of the fuel pellet. The fuel microstructure resembles the as-fabricated microstructure, showing extensive microcracking related to the phase transition at 450°C. Two types of secondary phases were observed, which could either be due to segregation and precipitation of fission products or to UN impurities from fabrication.

Finally, the current status of PIE on other ATF-1 irradiations will be discussed. These irradiations include UN-U_3Si_5 rodlets, UN-U_3Si_2 rodlets and an additional test with U_3Si_2 fuel.

INTENTIONALLY BLANK

CONTENTS

SUMMARY iii
1. INTRODUCTION 1
2. SUMMARY OF EXPERIMENTS AND IRRADIATION CONDITIONS 2
2.1 Experiments Test Matrix 2
2.2 Irradiation History 4
3. ATF-1G 9
3.1 Results from PIE 9
3.1.1 Visual inspection 9
3.1.2 Neutron Radiography 9
3.1.3 Dimensional Inspection 10
3.1.4 Gamma Spectrometry 12
3.1.5 Fission Gas Release 14
3.1.6 Optical Microscopy 15
3.1.7 Cladding microhardness 18
3.2 Discussion 20
4. ATF-73 21
4.1 Results from PIE 21
4.1.1 Visual inspection 21
4.1.2 Neutron Radiography 21
4.1.3 Gamma Spectrometry 22
4.1.4 Fission Gas Release 23
4.1.5 Optical Microscopy 23
4.2 Discussion 30
5. ATF-45 31
5.1 Results from PIE 31
5.1.1 Visual inspection 31
5.1.2 Neutron Radiography 32
5.1.3 Dimensional inspection 33
5.1.4 Gamma Spectrometry 34
5.1.5 Fission Gas Release 36
5.1.6 Optical Microscopy 36
5.1.7 Cladding Microhardness 39
5.2 Discussion 40
5.3 Other ATF-1 PIE 41
5.4 ATF-41 and ATF-44 41
5.5 ATF-10, ATF-30 and ATF-34 42

6. CONCLUSIONS 42
7. REFERENCES 44

FIGURES

Figure 1. (a) LHGR, (b) Fuel centerline temperature and (c) PICT for the ATF-1G rodlets. 5

Figure 2. LHGR for the 13H-cups of rodlet OF1. 6

Figure 3. (a) LHGR, (b) Fuel centerline temperature and (c) PICT for the ATF-1 LANL rodlets. 7

Figure 4. (a) LHGR, (b) Fuel centerline temperature and (c) PICT for the ATF-1 W01 and ATF-1WB rodlets. 8

Figure 5. Visual examination of rodlets (a) G01 and (b) G03. 9

Figure 6. (a) Thermal and (b) epithermal neutron radiographs of ATF-1GE rodlets. 10

Figure 7. Dimensional measurements of ATF-1G G01. The measured value represents the average of measurements taken every 5°. Red solid lines indicate the nominal values. 11

Figure 8. Dimensional measurements of ATF-1G G03. The measured value represents the average of measurements taken every 5°. Red solid lines indicate the nominal values. 11

Figure 9. Axial gamma scan of major fission products in rodlet G01. 12

Figure 10. Axial gamma scan of major fission products in rodlet G03. 12

Figure 11. Axial distribution of ^{54}Mn in the two ATF-1G rodlets. 13

Figure 12. Axial distribution of ^{60}Co in the two ATF-1G rodlets. 13

Figure 13. Gamma tomography of selected fission products for (a) G01 and (b) G03. 14

Figure 14. Radial cross section of G01 (50X). 15

Figure 15. Radial cross section of G03 (50X). 16

Figure 16. Example of localized porosity observed in the ATF-1G samples. 16

Figure 17. (a) Layer of secondary phases observed on the periphery of the fuel pellets. (b) and (c) highlight the increased thickness of the secondary phase layers close to large cracks open surfaces. (b) was taken from G01, while (c) from G03. 17

Figure 18. (a)-(b) Localized bonding observed in the sample from rodlet G01. 18

Figure 19. Microhardness profile across the cladding thickness for Alloy33® (G01). The red line represents the measured un-irradiated value and the uncertainty range [26]. 19

Figure 20. Microhardness profile across the cladding thickness for Kanthal APMT® (G03). The red line represents the measured un-irradiated value and the uncertainty range [26]. 19

Figure 21. Radial Cs distribution (yellow line) versus fuel local temperatures for average LHGR (blue lines) and maximum LHGR (red line) in G01. 20

Figure 22. Visual examination of rodlet OF1. 21

Figure 23. (a) Thermal and (b) epithermal neutron radiographs of rodlet OF1. 22

Figure 24. Axial gamma scan profile of the major fission products in rodlet OF1. 23

Figure 25. Axial gamma scan of activation products in the FeCrAl wafers and rodlets components. The distribution of a fission product, e.g., 106Ru, is also reported to show the local position of the fuel discs. 23

Figure 26. Retrieval of the H-cups in HFEF. 24

Figure 27. Low magnification image (50X) of the H-cup with C35M alloy, irradiated at different LHGR. (a) 196.75 W/cm (Position 1), (b) 135.11 W/cm (Position 13). 24

Figure 28. Low magnification image (50X) of the H-cup with C35M alloy pre-oxidized at 800°C, irradiated at different LHGR. (a) 187.60 W/cm (Position 2), (b) 138.90 W/cm (Position 12). The white arrows in (a) delimit the region where the fuel ceases to adhere to the FeCrAl discs. 25

Figure 29. Low magnification image (50X) of the H-cup with C35M alloy pre-oxidized at 1000°C, irradiated at different LHGR. (a) 183.70 W/cm (Position 3), (b) 143.36 W/cm (Position 11). 25

Figure 30. Low magnification image (50X) of the H-cup with C37M alloy pre-oxidized at 800°C, irradiated at 178.20 W/cm (Position 4). 26

Figure 31. Low magnification (50X) images of (a) B135Y3 (small grains) and (b) B135Y3 (large grains), both pre-oxidized. The LHGR was 148.27 W/cm (Position 10) and 157.90 W/cm (Position 8), respectively. 26

Figure 32. (a)-(c) H-cups corresponding to positions 5, 6 and 7. The specific ID of each cup is presently unknown. 27

Figure 33. High magnification image showing the UO_2-C35M interface. (a) Sample in Position 1, (b) Sample in Position 13. 28

Figure 34. High magnification image showing the UO_2-C35M interface. (a) Sample in Position 2, (b) Sample in Position 12. 28

Figure 35. High magnification image showing the UO_2-C35M interface. (a) Sample in Position 3, (b) Sample in Position 11. 28

Figure 36. (a) High magnification image showing the UO_2-C37M interface (Position 4). (b) Cracks observed along the C37M surface. 29

Figure 37. (a) Localized interaction and crack on the surface of the B135Y2 small grain sample (Position 10). (b) Surface irregularity on the interface between fuel and B135Y2 large grain sample (Position 8). Both samples were pre-oxidized. 29

Figure 38. (a) High magnification image of one of the unknown samples showing the appearance of the interface. (b) Localized surface defects observed outside the bonded region. 30

Figure 39. (a)-(b) Appearance of the interface of the other two unknown samples, respectively. 30

Figure 40. Visual examination of rodlet ATF-L45 32

Figure 41. (a) Thermal and (b) epithermal neutron radiographs of rodlet L45. 33
Figure 42. Angle-averaged profilometry measurements on ATF-L45. 34
Figure 43. Axial gamma spectrometry of ATF-L45 35
Figure 44. Axial gamma scan of the cladding activation product ^{54}Mn in ATF-L45. 35
Figure 45. Gamma tomography of selected fission products for ATF-L45. 36
Figure 46. Radial cross section of the UN-U_3Si_5 depleted pellet above the fuel stack of L45 (50X). 36
Figure 47. High magnification micrograph of the UN-U_3Si_5 structure. 37
Figure 48. Radial cross section of a U_3Si_5 pellet in the upper half of the fuel stack of L45 (50X). 37
Figure 49 Overview of the U_3Si_5 microstructure from the upper-half of the fuel column (a) Pellet center, (b) Pellet periphery. 38
Figure 50. Radial cross section of a U_3Si_5 pellet in the lower half of the fuel stack of L45 (50X). 38
Figure 51. Overview of the U_3Si_5 microstructure from the lower-half of the fuel column (a) Pellet center, (b) Pellet periphery. 39
Figure 52. Microhardness profile across the cladding thickness for Kanthal AF® 40
Figure 53. Thermal neutron radiography of the two capsules ATF-41 and ATF-44 41
Figure 54. Thermal neutron radiography of the two capsules ATF-10, ATF-30 and ATF-34. 42

TABLES

Table 1. Current status of PIE on ATF-1 capsules. 2
Table 2. Test matrix of the ATF-1G rodlets which have completed irradiation. 3
Table 3. Alloy ID of each H-cup part of rodlet ATF-OF1. 3
Table 4. Test matrix of the ATF-1 LANL rodlets which have completed irradiation. 4
Table 5. Test matrix of the ATF-1WB rodlets which have completed irradiation. 4
Table 6. Fission gas release, calculated average fuel centerline and burnup for ATF-1G 14
Table 7. Chemical composition of the released gas from ATF-1G rodlets. 15
Table 8. Fission gas release data, calculated temperature and burnup for ATF-L45. 36

Post-Irradiation Examination of the ATF-1 Experiments – 2019 Status

1. INTRODUCTION

The Accident Tolerant Fuels (ATF) Campaign continues to collaborate with industry and university partners to develop new Light Water Reactor (LWR) fuels that can offer enhanced accident tolerance during accidental scenarios as well as achievement of higher performance and burnup under operating conditions [1–3]. As the Campaign advances through Phase 2, the development and qualification phase, Post-Irradiation Examination (PIE) results from Phase 1, the feasibility assessment phase, continue to be collected on the ATF-1 capsules that have completed irradiation in the Advanced Test Reactor (ATR) at Idaho National Laboratory (INL). The aim of these drop-in capsule-type irradiation tests is to provide early screening of the proposed concepts. During the ATF-1 irradiation, fuel and cladding were placed in an outer capsule that provides isolation from the ATR reactor water coolant. The capsule acts as the primary safety barrier in case of cladding failure. While such irradiation configuration does not provide information regarding the interaction and compatibility of the cladding with reactor coolant, it offers assessment of fuel pellet performance and evaluation of potential fuel-cladding interaction with limited, but efficient investment.

The complete test matrix spans over a broad range of concepts, both evolutionary and revolutionary. While all concepts share the common objective of developing an alternative fuel/cladding system with enhanced performance compared to the standard UO_2-zircaloy system, each of them focuses on different aspects. For instance, concepts like U_3Si_2 or UO_2 plus highly conductive additives were explored to enhance thermal conductivity of the fuel, which is one of the main drawbacks of the current ceramic fuel. Other concepts were more focused on finding alternative claddings. In spite of the successful history of performance, Zr-alloy cladding suffers from severe limitations under both design-basis accidents (DBA) and beyond-design-basis accidents (BDBA) [4]. Many of the regulatory requirements and associated operational constraints are driven by failure risks associated with cladding embrittlement due to hydrogen pick-up and oxidation [5]. The large gain in the safety margin, which can be translated in economic benefit through increased operational flexibility, which is forecasted if these issues can be mitigated is a driving factor in current Research and Development (R&D) efforts aimed at developing and qualifying new cladding materials. Among others, advanced iron-based alloys proved to have desirable attributes in terms of improved oxidation resistance, which is a very favorable characteristic to increase coping time in DBA and BDBA. Such characteristic makes them promising candidates as accident tolerant cladding [4]. A variety of steel types have been tested under both accidental and normal operating conditions. Kanthal APMT® variants, commercial steels belonging to the SS-series and Fe-xCr (x = 15%, 20%, 25%) have been tested both in pure steam [6] or hydrogen-steam [7] environment showing improved corrosion resistance compared to Zr-2 and Zr-4. General Electric (GE) has selected two steels for applications in the ATF-1 irradiation, namely Alloy 33® and Kanthal APMT® [8]. The low burnup pins have completed irradiation and underwent PIEs, which are presented in Section 3. Oak Ridge National Laboratory (ORNL) has developed a test matrix comprising three rodlets dedicated to the assessment of chemical compatibility between UO_2 fuel and selected FeCrAl alloys [9,10]. The driving force behind this effort is the limited data available regarding the interaction between UO_2 and FeCrAl alloys under irradiation. The rodlets designed by ORNL will specifically study the phenomenon at different burnups. The low burnup pin has reached the burnup target in 2018 and underwent PIE, as presented in Section 4.

The ATF-1 capsules are also suitable for exploring actinide materials that could be envisioned as fuels if high enrichment could become a possibility for special reactor designs. The interest in exploring U_3Si_5 fuels stems from their potential use in composite fuels utilizing UN-U_3Si_5 matrix, which has been shown to have neutronic performance comparable to UO_2, but would allow a longer cycle length due to increased fuel loading [11], thus benefitting reactor operation and economics. Sintering nitride with

silicide offers the advantage of lowering the temperatures necessary for densification of UN by exploiting the "liquid phase sintering", as silicide compounds have a much lower melting temperature [12]. Relatively scarce data existed in literature even on the non-irradiated material before the experimental campaign undertaken at Los Alamos National Laboratory (LANL) [13–15]. A single preliminary neutron irradiation experiment has been conducted on U_3Si_5 in Argentina. No irradiation temperature is reported, but for the low displacements per atom (dpa) reached in that experiment (0.02 dpa), no significant changes in sample morphology and crystalline structure could be ascertained [16].

At the moment, the use of U_3Si_5 and UN-U_3Si_5 as fuel is hypothetical, but an early evaluation of their performance under irradiation conditions prototypical of Light Water Reactors (LWRs) provides a first insight on the material performance to guide future decisions for further development. PIE results of U_3Si_5 and UN-U_3Si_5 fuels with Kanthal AF® cladding are presented in Section 5 and Section 5.4, respectively.

UN-U_3Si_2 could offer similar advantages to UN-U_3Si_5 composites, but with even higher uranium loading in the silicide phase. Similar sintering methods have been used to fabricate these composites [17]. Two rodlets were received in the third quarter of this fiscal year and started non-destructive examinations (NDEs). The results, along with results for an additional U_3Si_2 pin received at the same time, are reported in Section 5.5.

2. SUMMARY OF EXPERIMENTS AND IRRADIATION CONDITIONS

2.1 Experiments Test Matrix

A summary of the ATF-1 irradiation device design was presented in Reference [18]. The complete test matrix part of the ATF-1 irradiation can be found in [19]. **Table 1** reports the current status of the PIE on the capsules currently located in the Hot Fuel Examination Facility (HFEF). Baseline NDEs include neutron radiography, gamma scanning and tomography, profilometry, and visual examination. Baseline destructive examinations include, but are not limited to, fission gas puncture, chemical burnup analysis, optical ceramography and microhardness testing.

Table 1. Current status of PIE on ATF-1 capsules.

Capsule ID	Fuel System	Concept Lead	Baseline Non-destructive	Baseline Destructive
ATF-00	UO_2 / Zr-4	Framatome	Completed	Completed
ATF-03	UO_2+ SiC / Zr-4	Framatome	Completed	Completed
ATF-04	UO_2+ diamond / Zr-4	Framatome	Completed	Completed
ATF-06	UO_2 / Alloy 33®	General Electric	Completed	On-going
ATF-08	UO_2 / Kanthal APMT®	General Electric	Completed	On-going
ATF-10	U_3Si_2 / Zirlo	Westinghouse	On-going	—
ATF-13	U_3Si_2 / Zirlo	Westinghouse	Completed	Completed
ATF-15	U_3Si_2 / Zirlo	Westinghouse	Completed	Completed
ATF-18	UO_2/ FeCrAl	ORNL	Completed	n.a.
ATF-30	UN-30%wt U_3Si_2 / Zirlo	Westinghouse	On-going	—
ATF-34	UN-30%wt U_3Si_2 / Zirlo	Westinghouse	On-going	—
ATF-41	UN- U_3Si_5 / Kanthal AF®	LANL	On-going	—
ATF-44	UN- U_3Si_5 / Kanthal AF®	LANL	On-going	—
ATF-45	U_3Si_5[a.] / Kanthal AF®	LANL	Completed	On-going
ATF-73	FCCI UO_2/FeCrAl	ORNL	Completed	On-going

a. The top and bottom pellets were UN with 15%volume U_3Si_5 loaded with depleted uranium.

Baseline PIE has been completed and reported previously for five capsules [20,21]. In addition, baseline NDEs were completed on ATF-18, which has been shipped this year for safety testing in the Severe Accident Test Station (SATS) at ORNL [22]. PIE on the four other capsules received in April 2018, namely ATF-06, ATF-08, ATF-45 and ATF-73, continued this year. Five other capsules (ATF-10, ATF-30, ATF-34, ATF-41 and ATF-44) were received in April 2019 and NDE commenced.

Four rodlets, designed to evaluate iron-based alloy performance were sponsored by General Electric. Commercial UO_2 fuel was used, and the emphasis is on the irradiation performance of the cladding alloys. The alloys selected were Alloy 33® and Kanthal APMT®, whose nominal compositions in weight percentage are 33 Cr + 32 Fe + 31 Ni + 1.6 Mo + 0.6 Cu + 0.4 N and 22 Cr + 5 Al + 3 Mo + Fe to balance, respectively. A total of four rodlets were assembled at INL, two for each type of material with two different burnup targets. Details about the two rodlets that have completed irradiation are reported in **Table 2**. The tests are collectively referred to as ATF-1G in this report.

Table 2. Test matrix of the ATF-1G rodlets which have completed irradiation.

Rodlet ID	Cladding Material	Fuel Material	Target Burnup (GWd/tHM)
G01	Alloy 33®	UO_2	20
G03	Kanthal APMT®	UO_2	20

ORNL Fuel-Cladding Chemical Interaction (FCCI) rodlets were developed based on a design resembling thermal diffusion-couples that are commonly used to study the interaction of two materials. The design incorporates several layers of cladding-UO_2 fuel specimens, enabling the test of different cladding materials and surface treatments within a single irradiation. The discs of FeCrAl and fuel are retained within an external ring which limits radial swelling of the UO_2 fuel as well as favors constant contact between the fuel and clad specimens, forming what is called an H-cup configuration [9]. Details about the composition of each H-cup content of the first rodlet are reported in **Table 3**. Some of the FeCrAl layers were pre-oxidized in order to form an oxide layer with different thickness in contact with the fuel. The scope is to study the effectiveness of an internal oxide layer to prevent chemical interaction between the fuel and the internal wall of the cladding.

Table 3. Alloy ID of each H-cup part of rodlet ATF-OF1.

Rodlet ID	Position	Alloy ID	FeCrAl Layer Status	Oxidation Temperature (°C) and Time (h)
ATF-OF1	1	C35M	As-machined	n.a.
	2	C35M	Oxidized	800°C/2h
	3	C35M	Oxidized	1000°C/2h
	4	C37M	Oxidized	1000°C/2h
	5	C37M	As-machined	n.a.
	6	APMT®	As-machined	n.a.
	7	B135Y2(LG)	As-machined	n.a.
	8	B135Y2(SG)	As-machined	n.a.
	9	B135Y2(LG)	Oxidized	1000°C/2h
	10	B135Y2(SG)	Oxidized	1000°C/2h
	11	C35M	Oxidized	1000°C/2h
	12	C35M	Oxidized	800°C/2h
	13	C35M	As-machined	n.a.

The test matrix led by LANL, called ATF-1 LANL, comprises three rodlets whose specifications are summarized in **Table 4**.

Table 4. Test matrix of the ATF-1 LANL rodlets which have completed irradiation.

Rodlet ID	Cladding Material	Fuel Material	^{235}U Enrichment (wt%)	Predicted Burnup (GWd/tHM)
L41	Kanthal AF®	UN-U_3Si_5	5.27	10
L44	Kanthal AF®	UN-U_3Si_5	2.69	7.5
L45	Kanthal AF®	U_3Si_5	8.83	13.2

Two irradiation campaigns were led by Westinghouse. The first one, the ATF-1W tests, comprising 6 rodlets in total, focused on the U_3Si_2-Zirlo system. Details about the composition of those rodlets have been reported elsewhere. PIEs on two of those rodlets were concluded last year [21]. An additional rodlet has been received and started PIE this year. A second irradiation campaign was led by Westinghouse, called ATF-1WB. UN-U_3Si_2 composite (30% wt U_3Si_2) with Zirlo cladding is the fuel system of these tests. Details are provided in **Table 5** for the rodlets that completed irradiation.

Table 5. Test matrix of the ATF-1WB rodlets which have completed irradiation.

Rodlet ID	Cladding Material	Fuel Material	Target Burnup (GWd/tHM)
WB2	Zirlo	UN-30% wt. U_3Si_2	20
WB6	Zirlo	UN-30% wt. U_3Si_2	20

2.2 Irradiation History

The irradiation history of all ATF-1 capsules is recorded in Reference [19]. Updated reports are issued at the end of each fiscal year, tracking the progress of each capsule. The heat generation and linear heat generation rate (LHGR) in each capsule are calculated using whole ATR core Monte Carlo (MCNP 6.0) simulations coupled with ORIGEN for depletion. The recorded ATR power history from each cycle and the initial ATR core loading are used as inputs to these simulations. The heat generation rates are then supplied to a finite element analysis code (Abaqus) to calculate the temperatures in the capsule. The axial variation in power is minimal, and temperature is only 10-20°C; therefore, only maximum centerline temperatures are reported here. The LHGR, fuel centerline temperature, and peak inner cladding temperature (PICT) histories are recorded in Figure 1 for the ATF-1G rodlets. Figure 2 reports the highest and lowest LHGRs, which correspond to the H-cups in position 1 and 13, respectively, in the ORNL OF1 rodlet. The other H-cups experienced LHGR intermediate to those reported in Figure 2. Figure 3 and Figure 4 show the irradiation histories of ATF-1 LANL and ATF-1WB. The irradiation history of rodlet W01, which was contained in capsule ATF-10, is also shown in Figure 4.

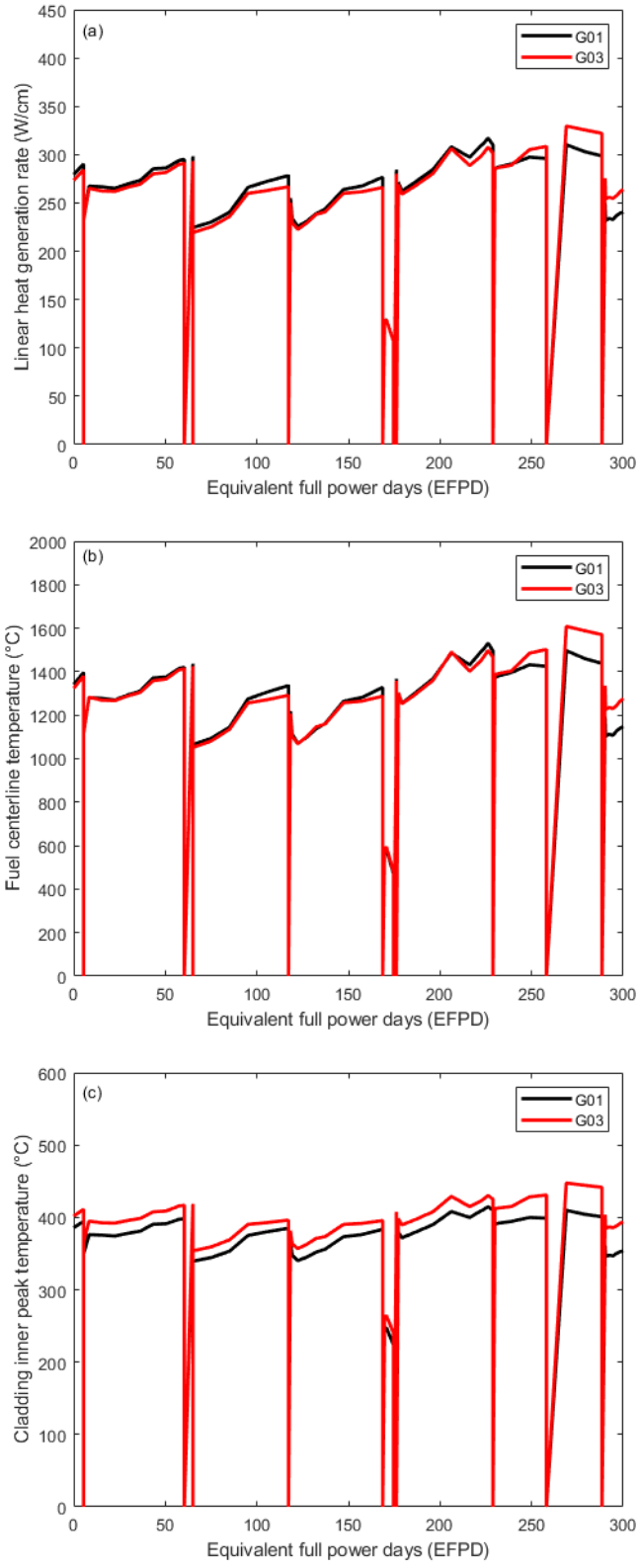

Figure 1. (a) LHGR, (b) Fuel centerline temperature and (c) PICT for the ATF-1G rodlets.

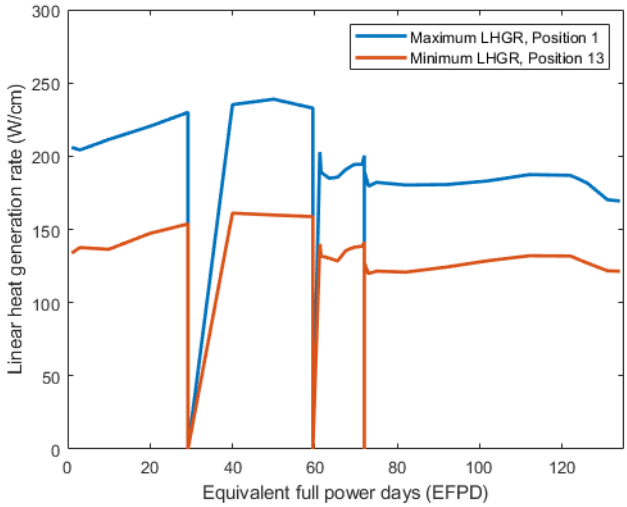

Figure 2. Maximum and minimum LHGR for the uppermost and lowermost H-cups of rodlet OF1.

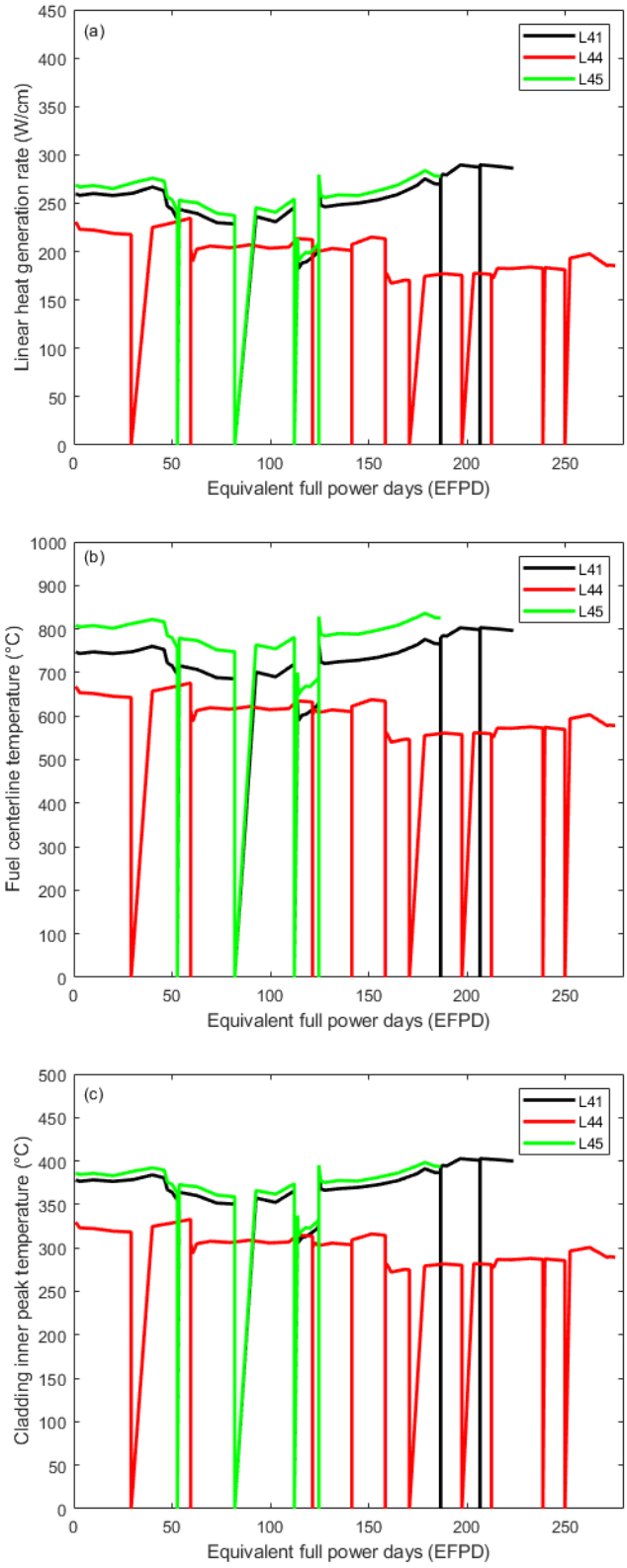

Figure 3. (a) LHGR, (b) Fuel centerline temperature and (c) PICT for the ATF-1 LANL rodlets.

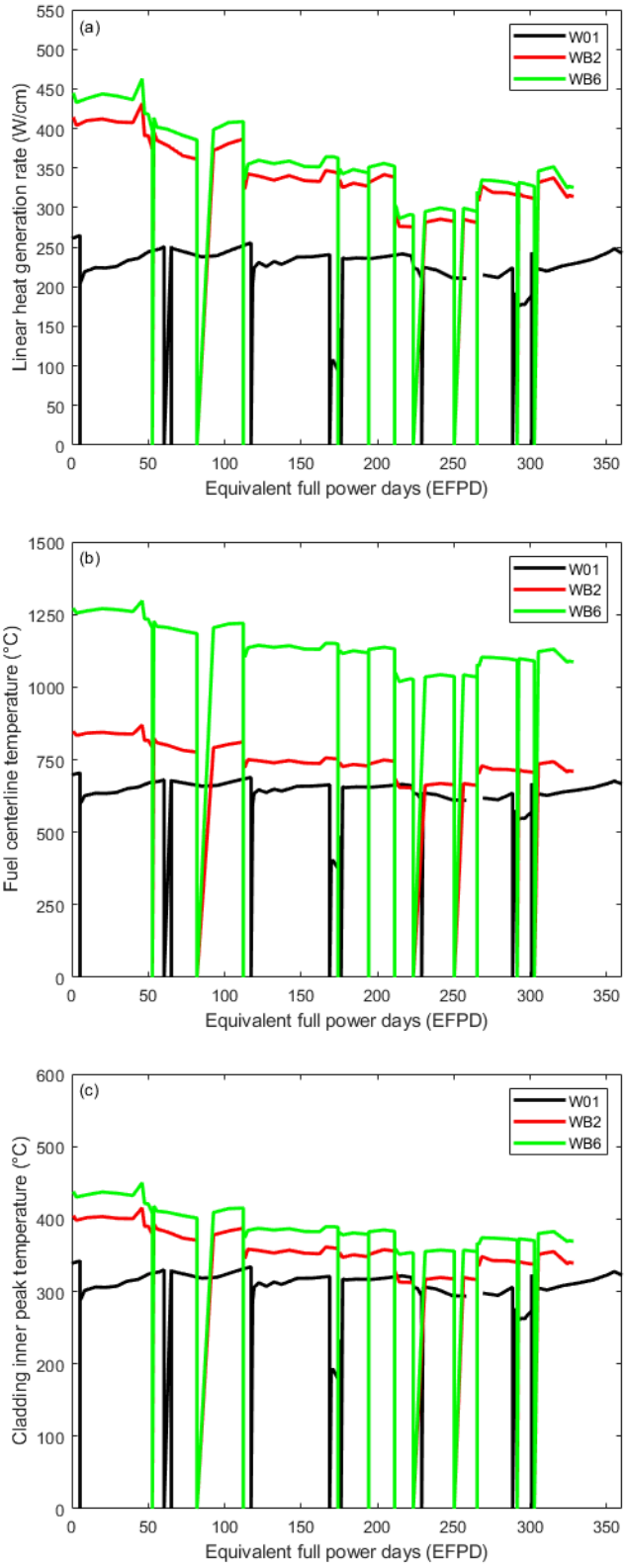

Figure 4. (a) LHGR, (b) Fuel centerline temperature and (c) PICT for the ATF-1 W01 and ATF-1WB rodlets.

3. ATF-1G

After the rodlets were irradiated at the ATR, PIE was performed at the INL HFEF. Baseline non-destructive PIE performed on the rodlets included visual inspection, neutron radiography, gamma spectrometry and tomography, and dimensional inspection. Details about the techniques can be found in [18]. After capsule examinations, capsule disassembly took place in the containment box in HFEF, and the rodlets underwent NDEs. After NDEs, cross-sections were cut from the mid-axial region of the rodlet to perform optical microscopy and microhardness.

3.1 Results from PIE

Prior to removing the rodlets from the capsules, visual examinations, neutron radiography, and axially resolved gamma spectrometry are performed on the intact capsules. Results from NDEs of the capsules can be found in the previous report [18]. The rodlets were then removed from the capsules, and PIE on the rodlets began.

3.1.1 Visual inspection

Visual inspection was performed on the rodlets at different azimuthal angles through the hot cell window. No unusual features were detected on the cladding surface. Representative pictures of the two rodlets are reported in Figure 5.

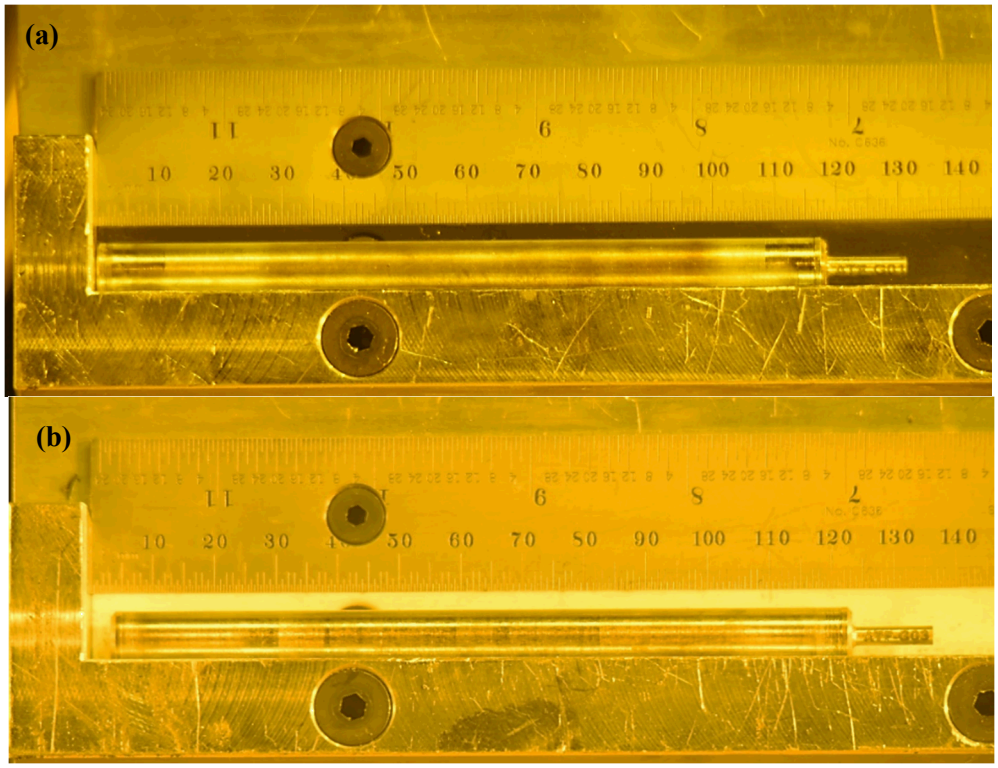

Figure 5. Visual examination of rodlets (a) G01 and (b) G03.

3.1.2 Neutron Radiography

Neutron radiography of the ATF-1G rodlets was performed using indirect radiography at the NRAD reactor located in HFEF [23]. Radiographs of the rodlets were taken at 6 different angles, each 30 degrees apart. The rodlet radiographs are shown in Figure 6, with the thermal neutron radiograph on the left and the epithermal neutron radiograph on the right. The bottom enriched pellet of the fuel stack in G03 looks severely fractured. The damage occurred during the capsule disassembly, as the neutron radiography of

the capsule showed that the pellet was intact [18]. Some cracking of the UO_2 pellet is visible along the full fuel stack, as normally occurs for ceramic fuels. No significant fuel relocation is observed, as expected. No significant axial growth was observed.

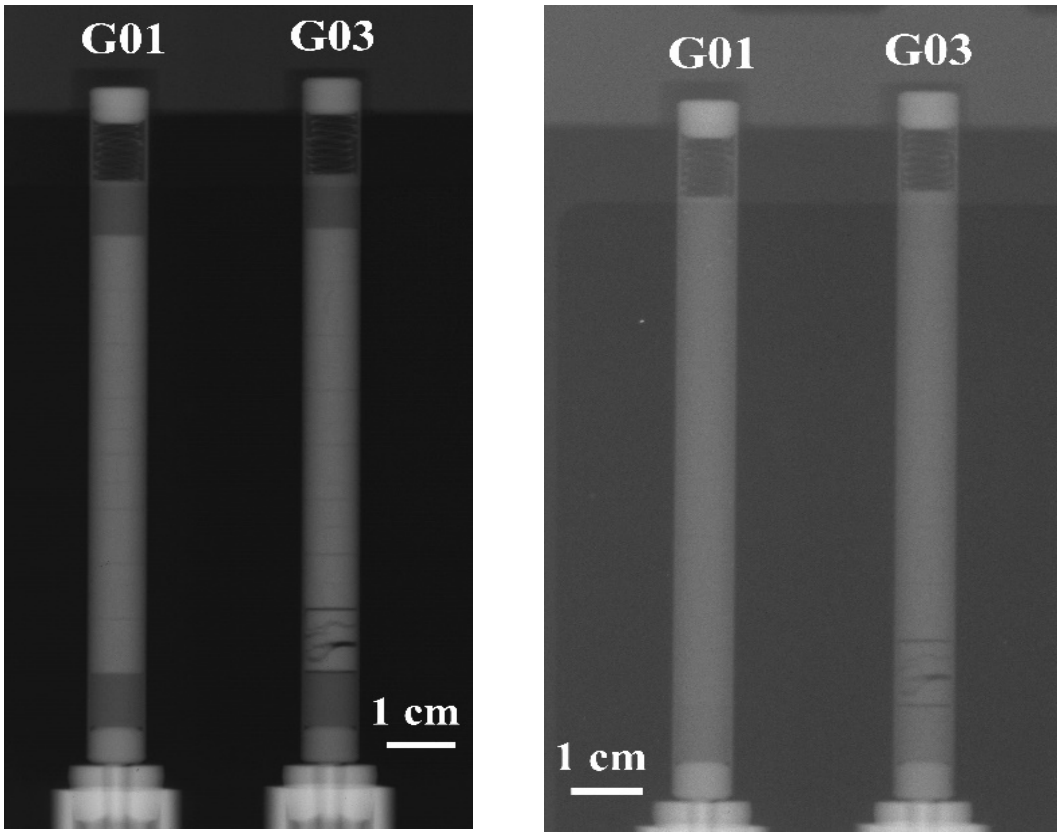

(a) **(b)**

Figure 6. (a) Thermal and (b) epithermal neutron radiographs of ATF-1GE rodlets.

3.1.3 Dimensional Inspection

Dimensional inspection of the ATF-1G rodlets was performed using a general purpose dimensional inspection device in HFEF. Outside diameter measurements were collected all along the rodlets in 0.5 mm increments axially and at 36 angles every 5 degrees from the initial scan angle to 180 degrees. Diameter measurements are collected with ±5 μm accuracy. The angle-averaged measured diameters for the ATF-1G rodlets is shown in Figure 7 for G01 and Figure 8 for G03. The specified cladding dimension is also shown, including fabrication uncertainty. No significant radial strain of the cladding, resulting in diametral change, was detected in either pins. The diameter value, when including the experimental uncertainty, is within the uncertainty of the as-fabricated values.

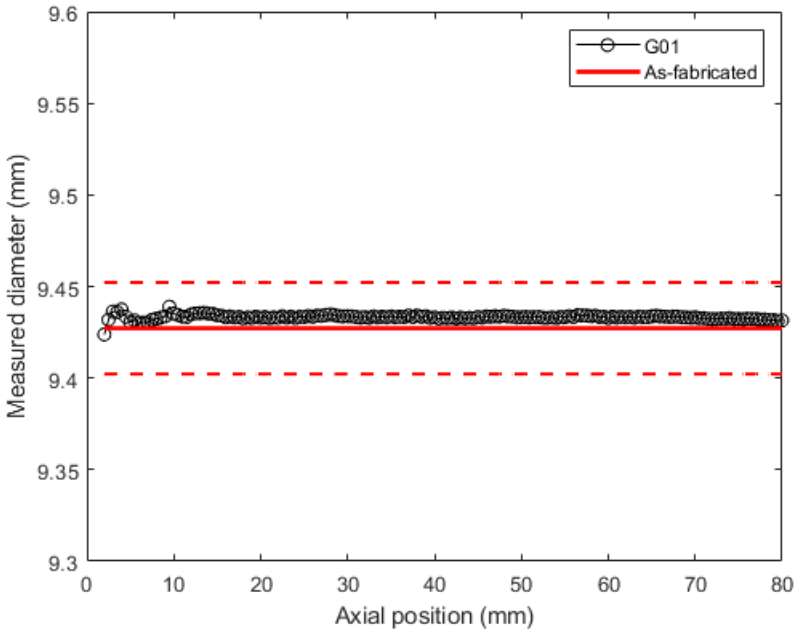

Figure 7. Dimensional measurements of ATF-1G G01. The measured value represents the average of measurements taken every 5°. Red solid lines indicate the nominal values.

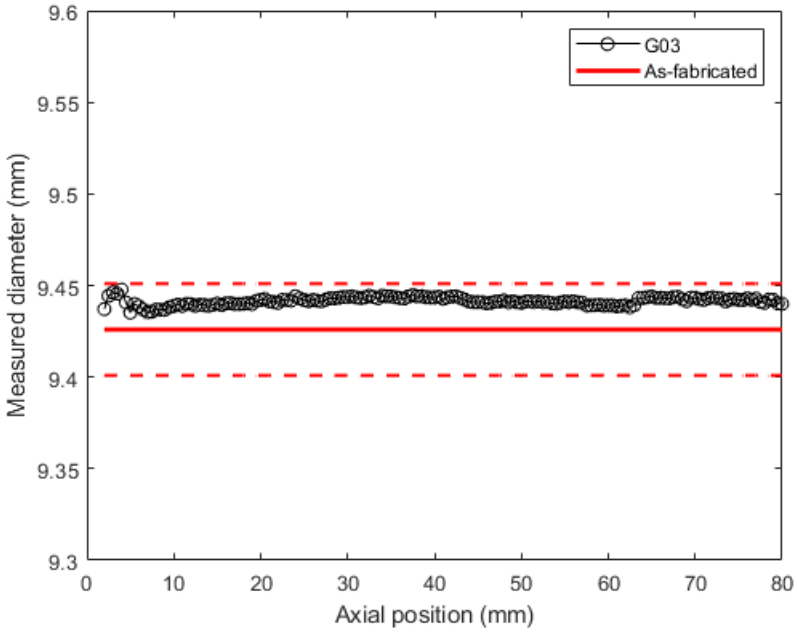

Figure 8. Dimensional measurements of ATF-1G G03. The measured value represents the average of measurements taken every 5°. Red solid lines indicate the nominal values.

3.1.4 Gamma Spectrometry

Gamma ray spectrometry of the two rodlets was performed using the HFEF Precision Gamma Scanner (PGS). The rodlets were scanned from bottom to top. Axial gamma spectrometry of all the rodlets showed that most detectable fission products did not redistribute axially. Examples of axial distribution of fission products, specifically ^{137}Cs, ^{154}Eu and ^{106}Ru, are reported in Figure 9 and Figure 10 for G01 and G03, respectively. The signal depression at the top and bottom of the fuel stack corresponds to the location of depleted uranium end-pellets. In Figure 11 and Figure 12, some of the activation products, typically created in ferritic steels, are shown. ^{54}Mn is produced from absorption of fast neutrons on ^{54}Fe. As both rodlets experienced similar neutron flux, the higher concentration of ^{54}Mn in rodlets G03 depends mostly on the different initial compositions of the two claddings. ^{60}Co is formed from activation of Ni and Co impurities. The high counts above and below the fuel stack stem from the stainless steel used for welding caps and spring. Increased ^{60}Co activity can be seen in G01, reflecting the Ni content of this alloy.

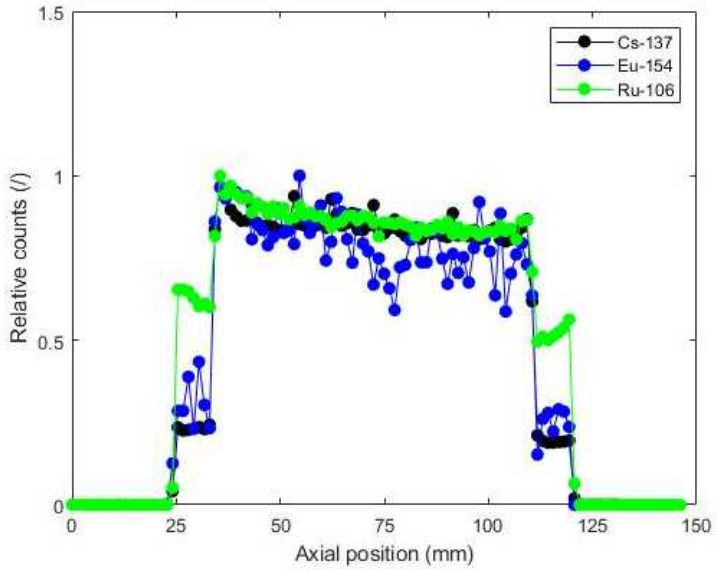

Figure 9. Axial gamma scan of major fission products in rodlet G01.

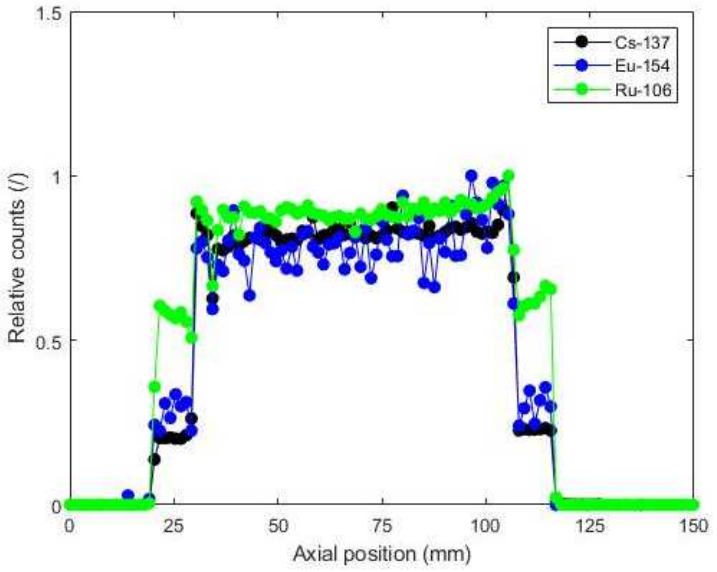

Figure 10. Axial gamma scan of major fission products in rodlet G03.

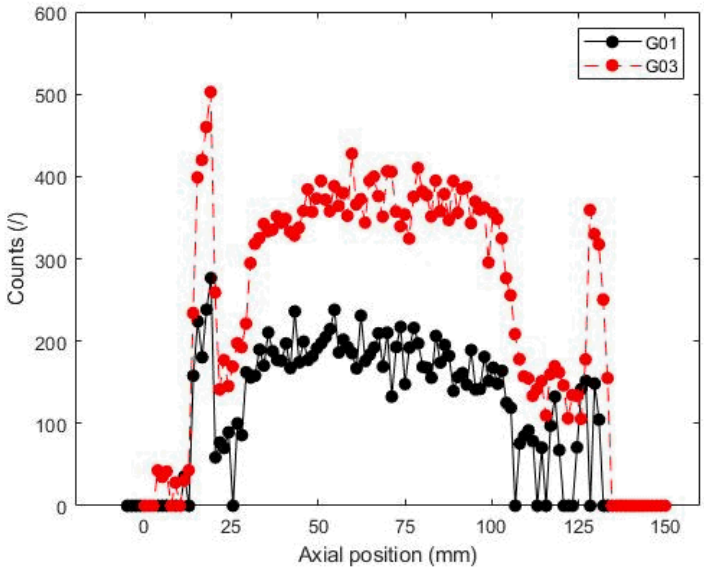

Figure 11. Axial distribution of ^{54}Mn in the two ATF-1G rodlets.

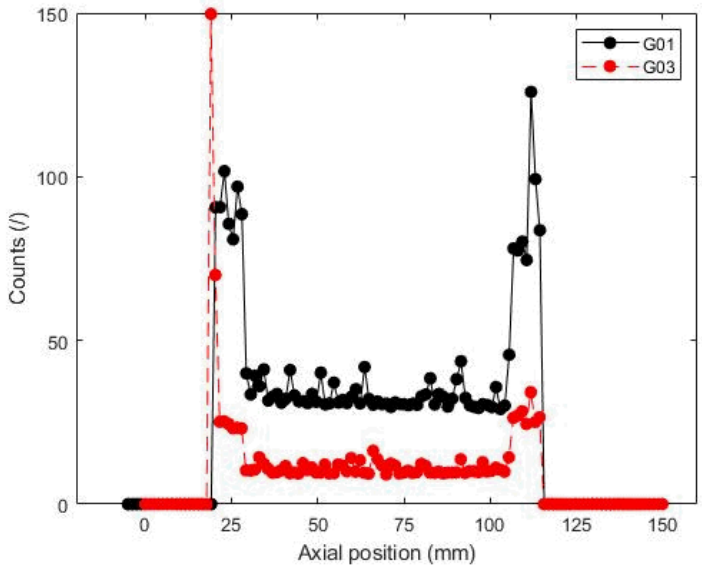

Figure 12. Axial distribution of ^{60}Co in the two ATF-1G rodlets.

In addition to axial gamma spectrometry scans, it is possible to collect two-dimensional distribution of fission products over a specific axial location. This is referred to as Gamma Emission Computed Tomography (GECT), whose details can be found elsewhere [24].

Gamma tomography results of specific fission products are shown in Figure 13. The results are similar for both rodlets. Generally, 16 different angles are collected to obtain the tomography reconstruction, but, for rodlet G03 only 13 angles could be collected due to a system malfunction. This partially impacted the quality of the reconstructed images in Figure 13b, which have increased noise level compared to the results in Figure 13a. Fission products and their daughters that are generally immobile in the fuel matrix, such as ^{144}Ce and ^{95}Nb [25], are homogeneously distributed across the radius. The slight enrichment of the burnup monitors ^{144}Ce and ^{95}Nb is consistent with the increased burnup on the pellet rim of LWR fuels. The volatile fission product ^{137}Cs shows depletion in the pellet central part for each of the rodlets. Similar results were observed for ^{134}Cs. The behavior is further analyzed in Section 3.2.

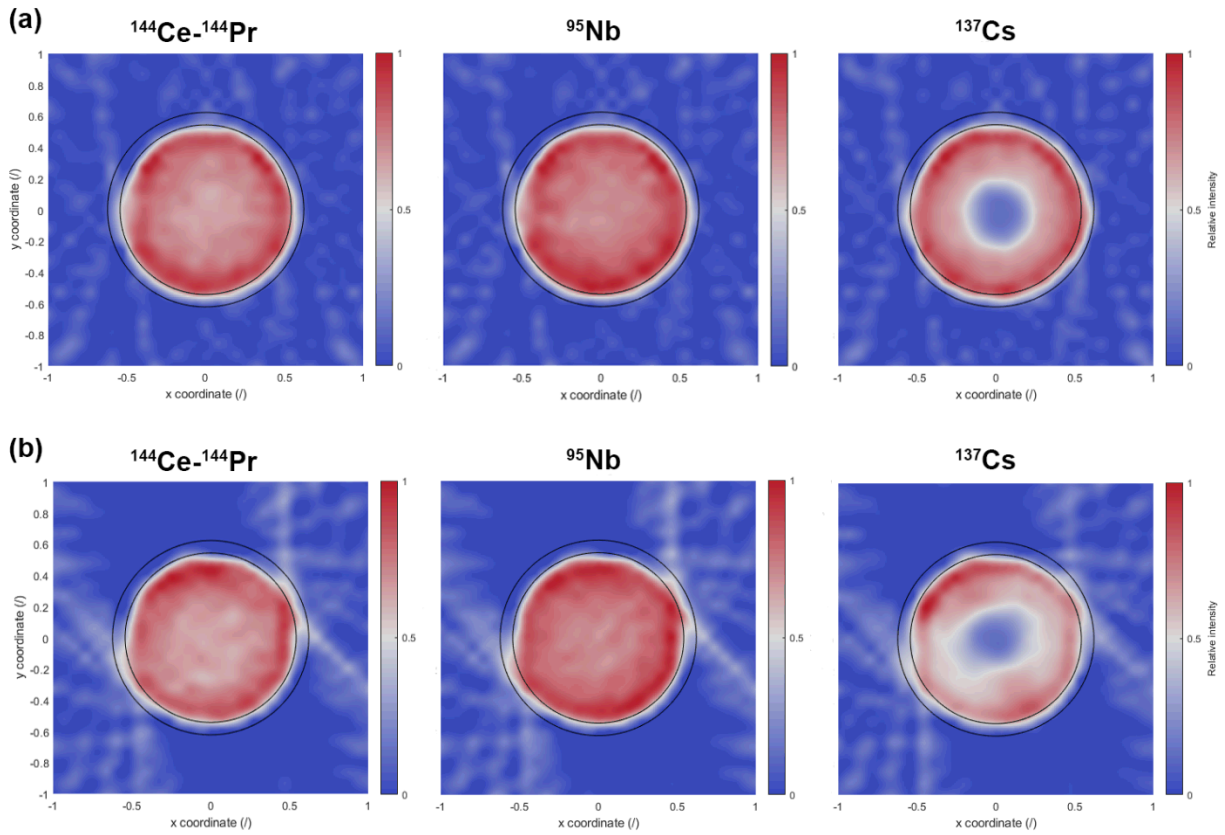

Figure 13. Gamma tomography of selected fission products for (a) G01 and (b) G03.

3.1.5 Fission Gas Release

Fission gases were collected from the rodlets using the HFEF Gas Assay, Sample, and Recharge (GASR) system. Rodlets were punctured using a 150 W Nd-YAG laser system, and a gas sample was collected in a stainless steel bottle external to the hot cell. Void volume in the rodlet was then determined by a series of backfills into the punctured rodlet and expansions into the GASR system. The rodlet internal gas pressure was derived from the void volume measurement and the initial gas pressure measurement upon puncture. Fission gas compositional analysis was performed by gas mass spectrometry. Results of fission gas analysis provided total elemental composition, krypton isotopic composition, and xenon isotopic composition.

Table 6 summarizes the average calculated fuel centerline irradiation temperature, calculated burnup and fission gas release (FGR) of the two rodlets. **Table 7** reports the composition of the detected gas.

Table 6. Fission gas release, calculated average fuel centerline and burnup for ATF-1G.

Rod ID	Fuel Centerline Average Temperature (°C)	Burnup (GWd/tHM)	Fission Gas Release (%)
G01	1253	18.3	7.06 ±0.21
G03	1270	18.3	5.85 ± 0.12

Table 7. Chemical composition of the released gas from ATF-1G rodlets.

Rod ID	Kr (%)	Xe (%)	H_2 (%)	He (%)	N (%)	O (%)	Ar (%)	CO_2 (%)	Other Gases (%)
G01	8.480	59.800	0.651	28.600	1.380	0.074	0.184	0.785	0.046 ±0.005
	±0.03	±0.4	±0.01	±0.4	±0.06	±0.007	±0.04	±0.05	
G03	7.710	54.300	0.451	36.400	0.140	0.013	0.190	0.710	0.086 ±0.002
	±0.05	±0.4	±0.007	±0.4	±0.01	±0.004	±0.001	±0.003	

3.1.6 Optical Microscopy

Microscopy samples for investigation of the microstructure were prepared using standard metallographic techniques and examined by a Leica DMi8 microscope installed in the HFEF hot cell. One transverse cross section was prepared from each rodlet, cut from the mid axial position. Mounts overviews from optical microscopy of the pins are shown in Figure 14 and Figure 15. Both pellets are extensively cracked, and the gap appears almost closed. Some areas appear to have high localized porosity (see Figure 16). From the morphology, it is likely that those are a consequence of fabrication inhomogeneities.

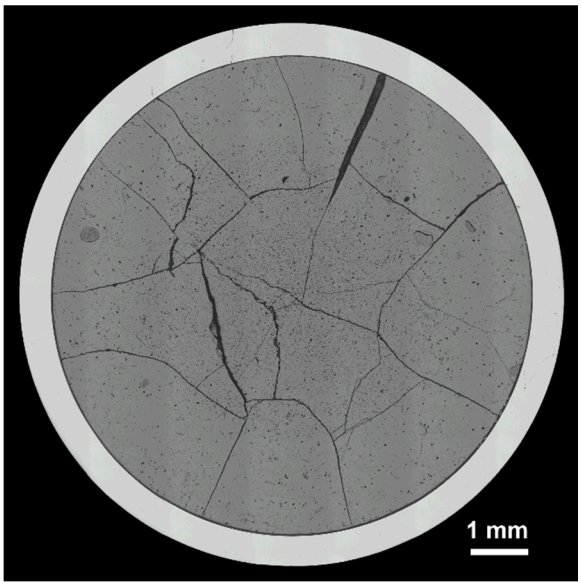

Figure 14. Radial cross section of G01 (50X).

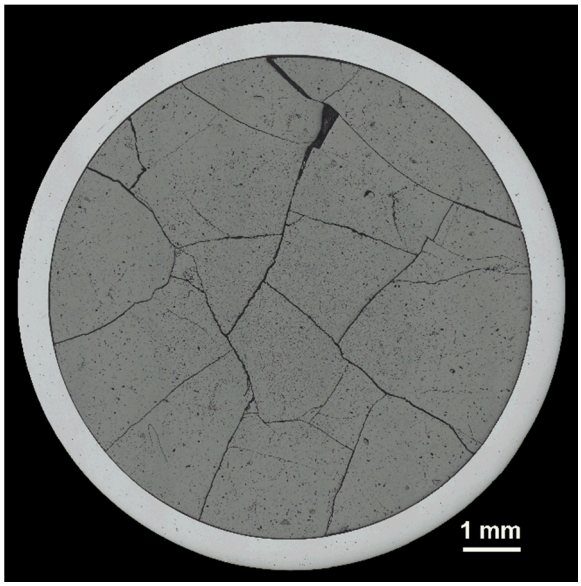

Figure 15. Radial cross section of G03 (50X).

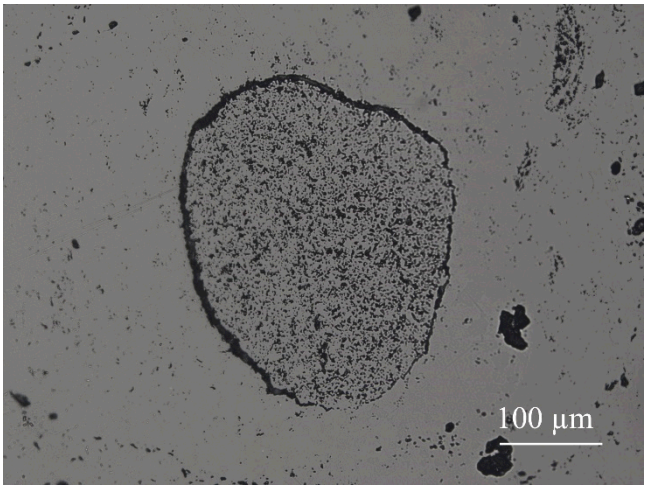

Figure 16. Example of localized porosity observed in the ATF-1G samples.

Secondary phases were observed along the pellet periphery of both rodlets. A representative example is shown in Figure 17a. The thickness of the secondary phase layer increases drastically on the open surface of large cracks, as shown in Figure 17b and Figure 17c. No fuel-cladding bonding layer was detected, other than in specific locations in pin G01 as shown in Figure 18. Other than the two specified locations, the cladding inner surface appeared intact and free of wastage, excluding severe corrosion due to the secondary phases or chemical interaction with the fuel.

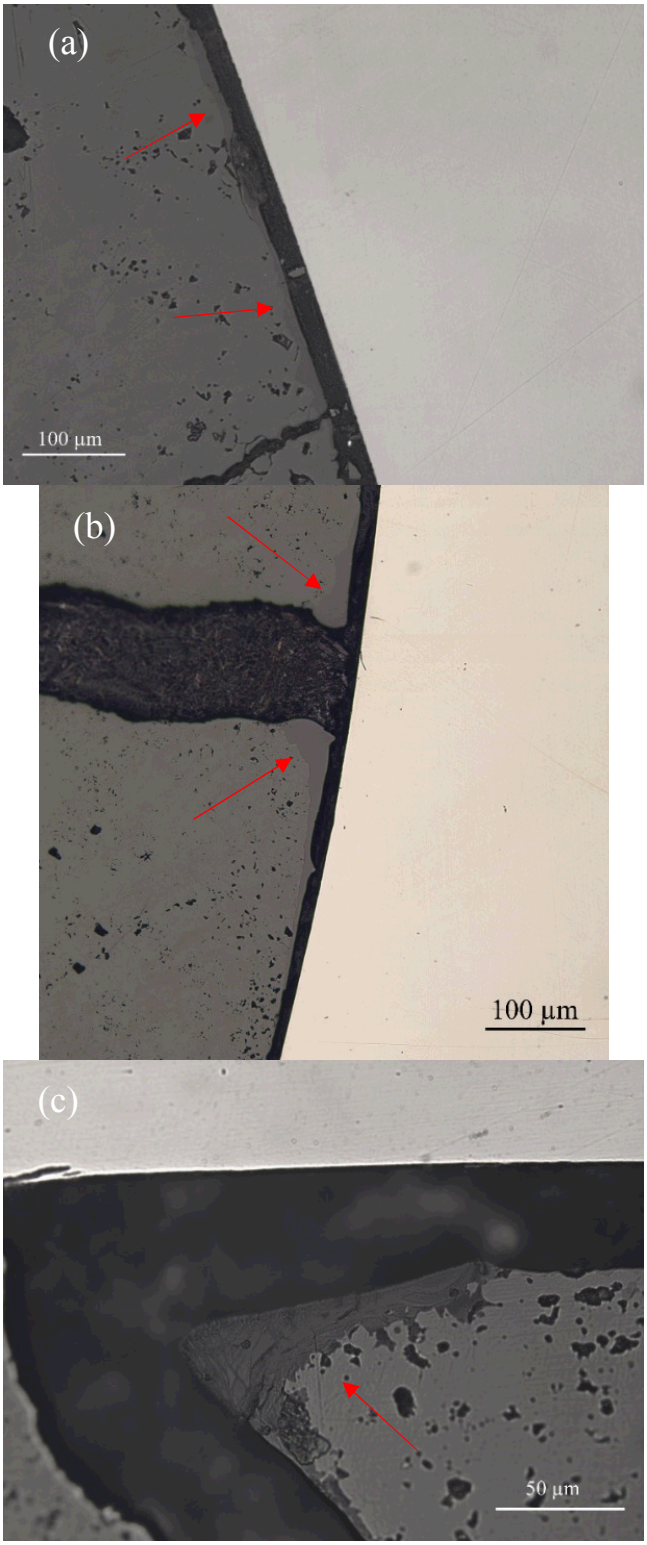

Figure 17. (a) Layer of secondary phases observed on the periphery of the fuel pellets. (b) and (c) highlight the increased thickness of the secondary phase layers close to large cracks open surfaces. (b) was taken from G01, while (c) from G03.

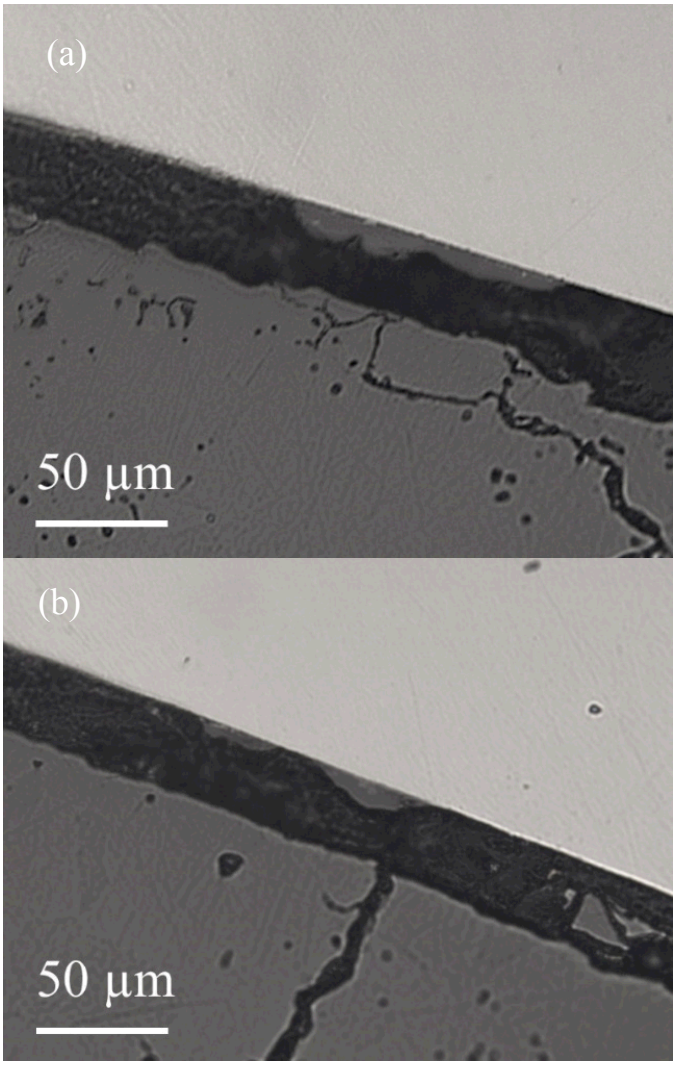

Figure 18. (a)-(b) Localized bonding observed in the sample from rodlet G01.

3.1.7 Cladding microhardness

Vickers microhardness measurements were carried out using a LECO AMH55 microscope equipped with a Micro/Macro Vickers Hardness Testing System. The measurements were performed at room temperature under argon protective atmosphere with a load of 50 gf. Dwell time was 13 s. The Vickers hardness number was computed as follows,

$$HV_{0.5} = 0.0018544\frac{P}{d^2} \quad (1)$$

where P (gf) is the applied maximum load and d (µm) is the average length of the two diagonals of the indentation prints. The hardness value was calculated from the average of five indentations at each position along the cladding thickness [26].

Figure 19 and Figure 20 show the profile of the measured Vickers number for Alloy33® (G01) and Kanthal APMT® (G03), respectively. The average Vickers hardness number for the unirradiated alloys is reported along with the uncertainty range [27]. No significant hardening of the alloys was measured. Indentations were made on the zone close to the areas showing significant formation of the secondary phases shown in Figure 17. No local increase in the cladding hardness was measured in the zone.

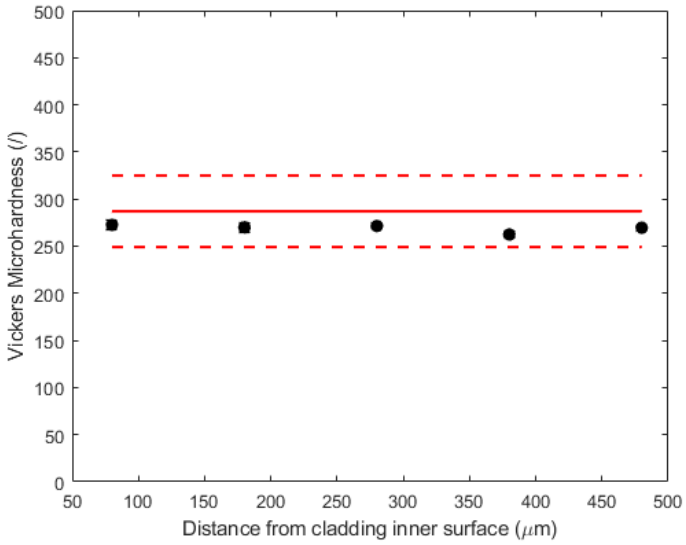

Figure 19. Microhardness profile across the cladding thickness for Alloy33® (G01). The red line represents the measured un-irradiated value and the uncertainty range [27].

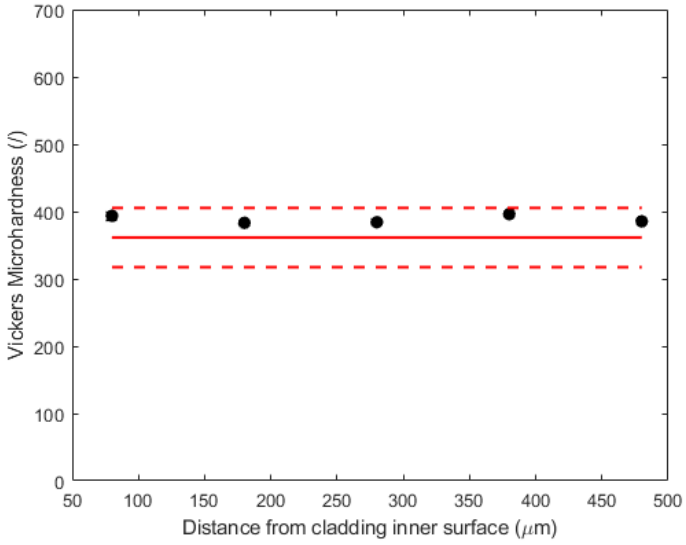

Figure 20. Microhardness profile across the cladding thickness for Kanthal APMT® (G03). The red line represents the measured un-irradiated value and the uncertainty range [27].

3.2 Discussion

Visual inspection and neutron radiography revealed no anomalies in the ATF-1G rodlets examined to date. Both rodlets experienced very similar irradiation conditions, other than during the last cycle (see Figure 1a). The higher linear power of G03 resulted in a difference of approximately 42°C between the fuel centerline temperatures towards the end of irradiation (Figure 1c). The FGR from G03 was expected to be higher than for G01, as the latter has experienced higher irradiation temperatures. The data in **Table 6** show the opposite trend. No obvious differences that could explain the higher FGR (e.g., pronounced cracking) were observed in the microstructure of G01 from optical microscopy. Presently, the observed behavior is not understood, and further analyses are needed.

The higher retained gas in G03, resulting in enhanced swelling compared to G01, could be the reason for the higher hoop strain, which is given by the relative diameter change, observed for the Kanthal cladding (see Figure 8 vs Figure 7). The hoop strain for G03 has an average value of 0.16%, while G01 hoop strain remained below 0.04%. In both cases, the hoop strain is limited.

While axial gamma scanning did not reveal any axial redistribution of fission products (Figure 9 and Figure 10), tomography showed extensive Cs radial migration. The absence of axial redistribution is explained by the lack of large axial thermal gradients occurring in such short pins. Cs release from the central part of the pellet is due to thermally driven diffusion and release. For G01, Cs relative activity is plotted radially against predicted BISON fuel local temperatures [28] in Figure 21. The blue curve represents the fuel temperatures for average LHGR, while the red curve represents the fuel local temperatures for the maximum LHGR. The Cs-depleted region has experienced temperatures exceeding ≈1200°C. Walker et al. [29], performed Electron Probe Micro Analysis (EPMA) on ramp-tested UO_2 fuels and showed that the onset and completion of cesium release corresponded to the 1200°C and 1550°C radial isotherms, respectively [29]. The present results are consistent with what was observed by Walker.

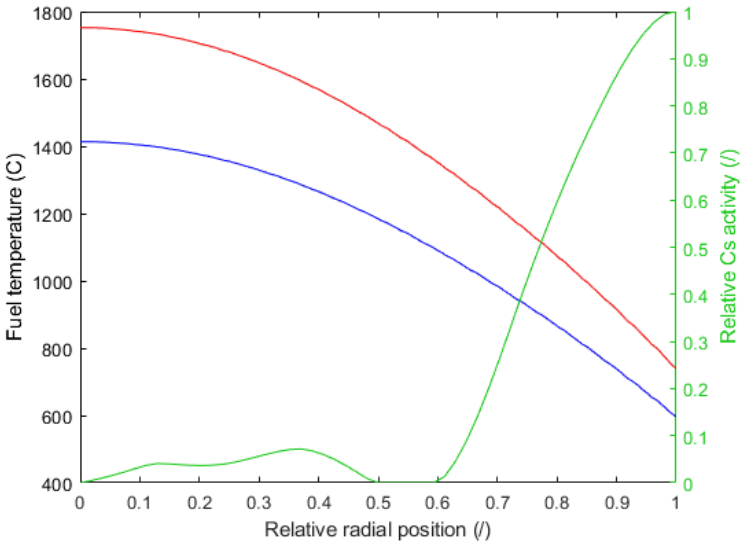

Figure 21. Radial Cs distribution (green line) versus fuel local temperatures for average LHGR (blue line) and maximum LHGR (red line) in G01.

In G01, a layer of secondary phases was observed along the pellet periphery, with increasing thickness corresponding to fuel cracks (Figure 17). The inner surface of the cladding does not show corrosion detectable via optical microscopy, even in the region adjacent to the large deposits. Local

microhardness measurements have been performed in the cladding adjacent to the region shown in Figure 17b, and no localized hardness increase was measured, excluding cladding embrittlement following secondary phases attack. Similarly, a layer of secondary phases was observed along the fuel periphery of G03. It is not known if these phases are a result of cladding components diffusing into the fuel (e.g., Cr or Al) or could be cesium uranate [30] forming after accumulation on the pellet periphery of volatile cesium migrated from the central part of the pellet (Figure 18). Energy Dispersive X-Ray (EDX) analyses are necessary to determine the chemical composition of these phases.

4. ATF-73

4.1 Results from PIE

Non-destructive examinations on the capsule were completed last fiscal year, showing no major defects in the rodlet. The capsule was punctured to verify whether the rodlets had leaked, and no fission gas was detected in the capsule. After removal from the capsule, the series of NDEs were conducted.

4.1.1 Visual inspection

Visual inspection was performed together with the ATF-1G rodlets and ATF-L45, and an example is shown in Figure 22. No unusual features were observed on the tube surface.

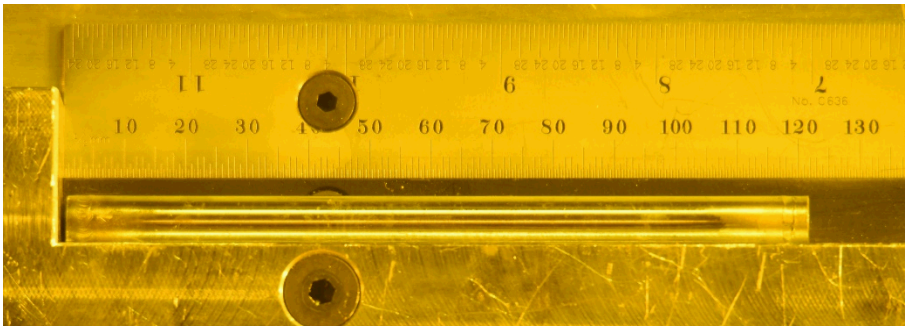

Figure 22. Visual examination of rodlet OF1.

4.1.2 Neutron Radiography

Neutron radiography is shown in Figure 23. The thirteen bright discs in Figure 23a correspond to the UO_2 discs. The FeCrAl discs surrounding the pellet discs are evident in Figure 23b. The radiographs provide evidence that the H-cups are intact in the external tube. At the top of the spring, the SiC thermometry disc is visible in both radiographs. The SiC thermometry discs at the top of the fuel stack and below the zirconia insulator pellet are visible, but not clearly distinguishable.

Figure 23. (a) Thermal and (b) epithermal neutron radiographs of rodlet OF1.

4.1.3 Gamma Spectrometry

Axial gamma scans are reported in Figure 24 and Figure 25. Figure 24 shows 13 sharp peaks localizing the UO_2 discs. For each disc, the relative profile of the major fission product monitor is consistent, suggesting minor burnup variations among the discs. In Figure 25 a fission product profile is superimposed to the profile of iron-alloy activation products. For each peak corresponding to the fission products, two peaks from the FeCrAl coins in each H-up are visible. In addition, ^{60}Co profile is reported too, showing the position of the spring.

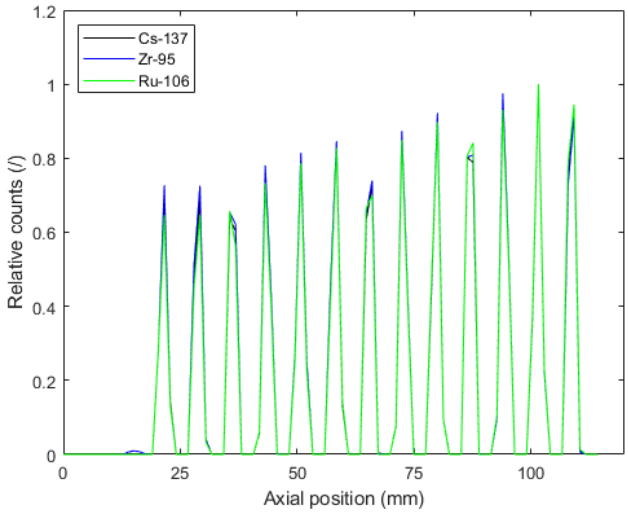

Figure 24. Axial gamma scan profile of the major fission products in rodlet OF1.

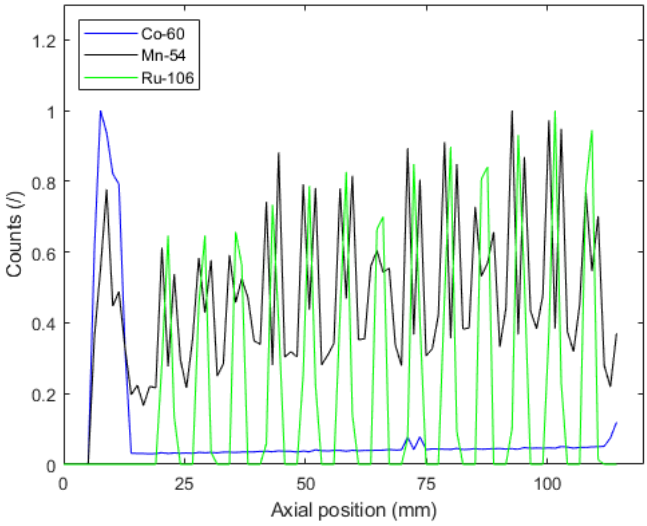

Figure 25. Axial gamma scan of activation products in the FeCrAl wafers and rodlets components. The distribution of a fission product, e.g., ^{106}Ru, is also reported to show the local position of the fuel discs.

4.1.4 Fission Gas Release

The rodlet was punctured with the GASR system. Fission gas release was calculated to be 6.10% ±0.10% of the initial inventory.

4.1.5 Optical Microscopy

Before microscopy could be performed, each H-cup had to be retrieved from the rodlet and prepared in a single mount. Retrieval of the H-cups was performed in the containment box of HFEF (Figure 26). After the extraction, the H-cup was mounted with faces perpendicular to the mount observation plane, ground and polished to mid-plane to reveal the UO_2-FeCrAl interfaces. Examination was performed with a Leica DMi8 microscope installed in the hot cell. Extraction of 10 out of 13 H-cups was successful. The last three were stuck in the rodlet and could be extracted only with energetic shaking of the rodlet. During

retrieval process, the cups corresponding to positions 5, 6 and 7 (see Table 3) got mixed. As the external H-cup has no identification mark, it is not possible to certainly assign the identification numbers to those three samples. EDX analyses are necessary to assign each mount to the original rodlet position based on the chemical composition of the FeCrAl coins. The H-cup corresponding to position 9 fell out of the mount during polishing process. The sample has been retrieved and is currently being re-prepared for analysis.

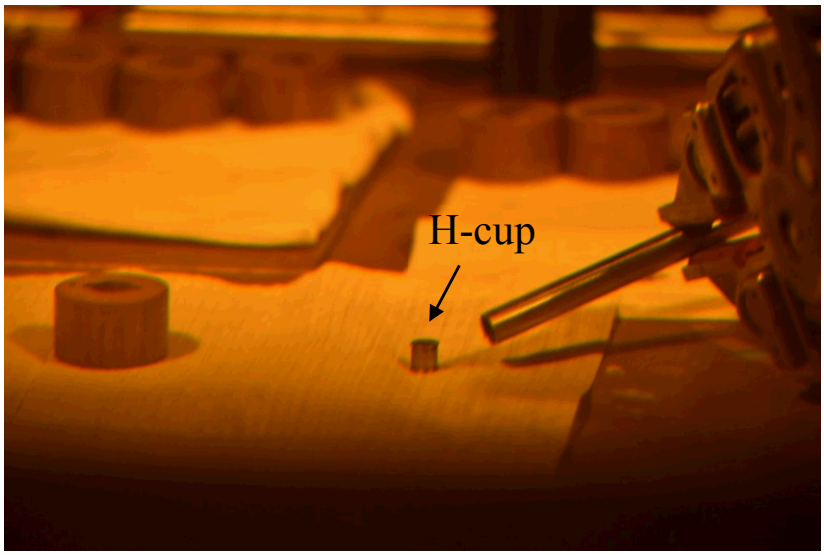

Figure 26. Retrieval of the H-cups in HFEF.

Overview of the H-cups is shown in Figure 27 through Figure 32. Most of the fuel-coins interface showed no extensive interaction, but localized defects were occasionally observed. Examples of the interfaces and the defects are shown in high magnification images in Figure 33 through Figure 39.

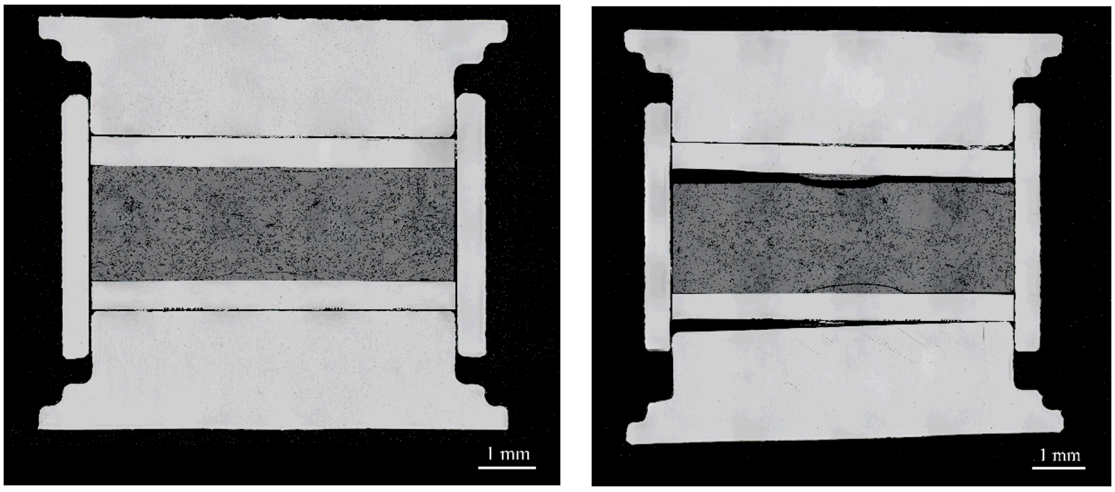

(a) **(b)**

Figure 27. Low magnification image (50X) of the H-cup with C35M alloy, irradiated at different LHGR. (a) 196.75 W/cm (Position 1), (b) 135.11 W/cm (Position 13).

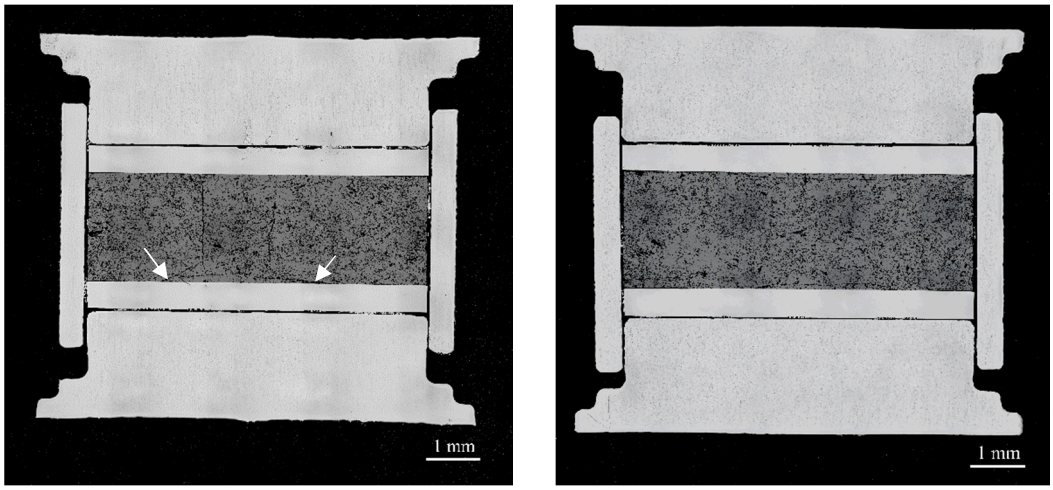

(a) **(b)**

Figure 28. Low magnification image (50X) of the H-cup with C35M alloy pre-oxidized at 800°C, irradiated at different LHGR. (a) 187.60 W/cm (Position 2), (b) 138.90 W/cm (Position 12). The white arrows in (a) delimit the region where the fuel ceases to adhere to the FeCrAl discs.

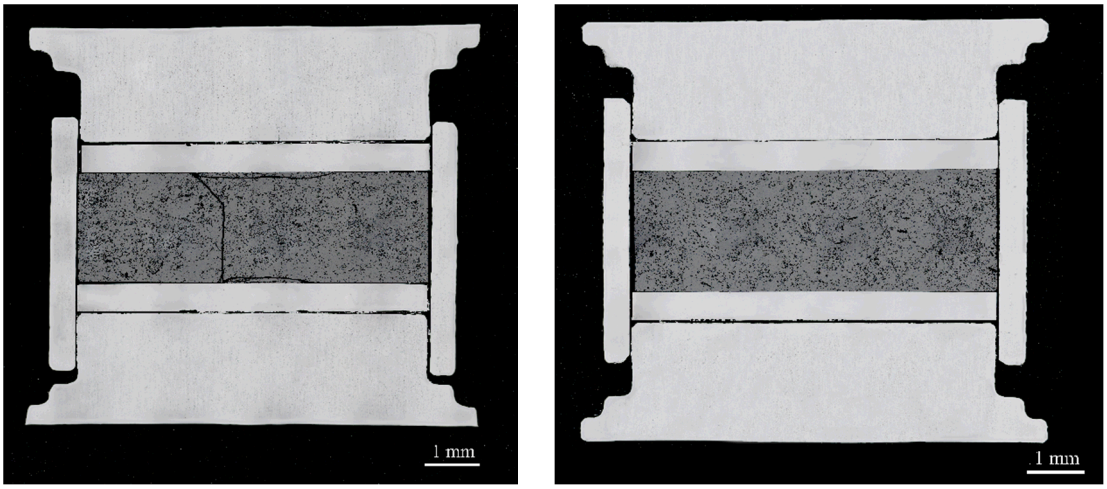

(a) **(b)**

Figure 29. Low magnification image (50X) of the H-cup with C35M alloy pre-oxidized at 1000°C, irradiated at different LHGR. (a) 183.70 W/cm (Position 3), (b) 143.36 W/cm (Position 11).

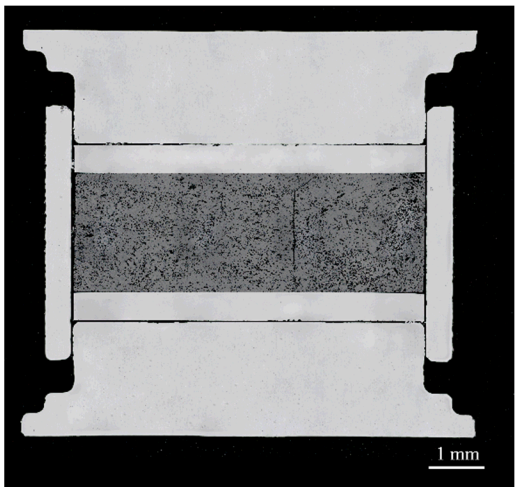

Figure 30. Low magnification image (50X) of the H-cup with C37M alloy pre-oxidized at 1000°C, irradiated at 178.20 W/cm (Position 4).

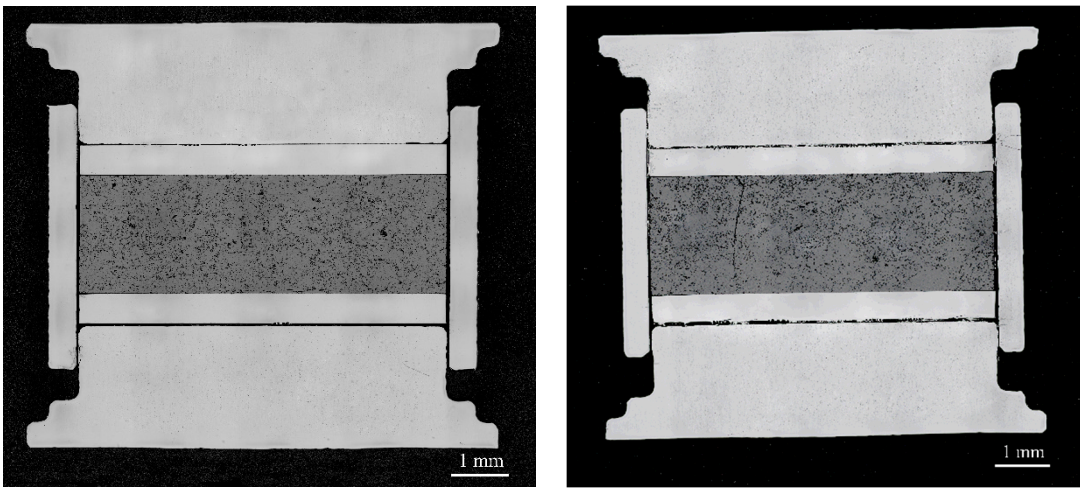

(a) **(b)**

Figure 31. Low magnification (50X) images of (a) B135Y3 (small grains) and (b) B135Y3 (large grains), both pre-oxidized. The LHGR was 148.27 W/cm (Position 10) and 157.90 W/cm (Position 8), respectively.

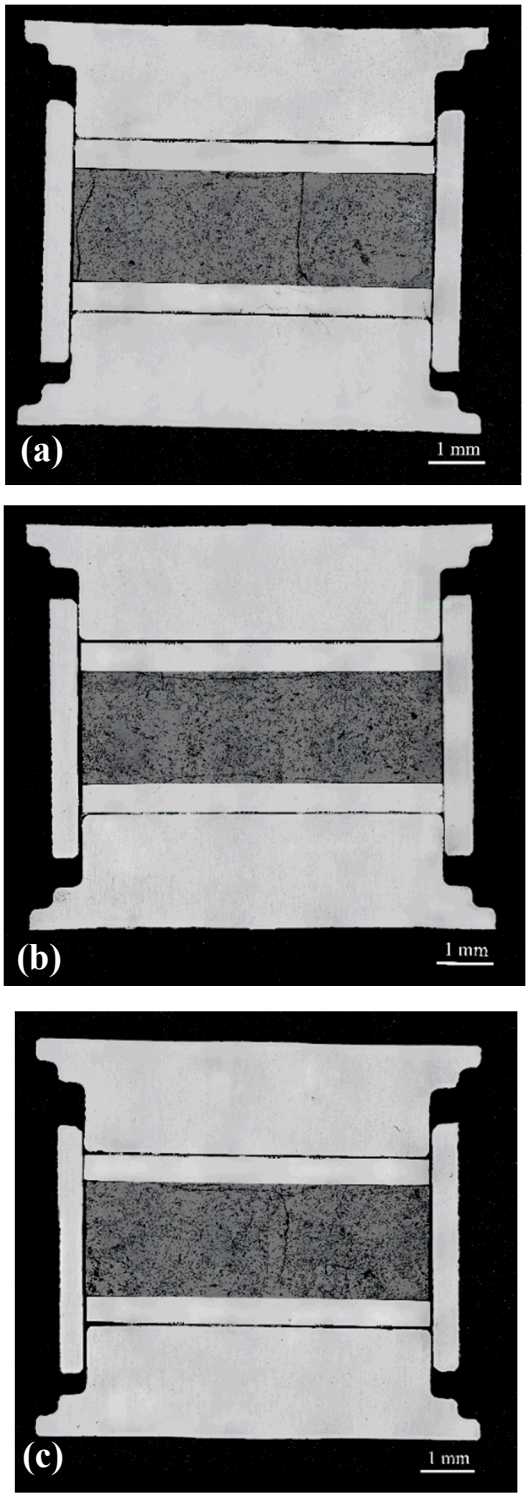

Figure 32. (a)-(c) H-cups corresponding to positions 5, 6 and 7. The specific ID of each cup is presently unknown.

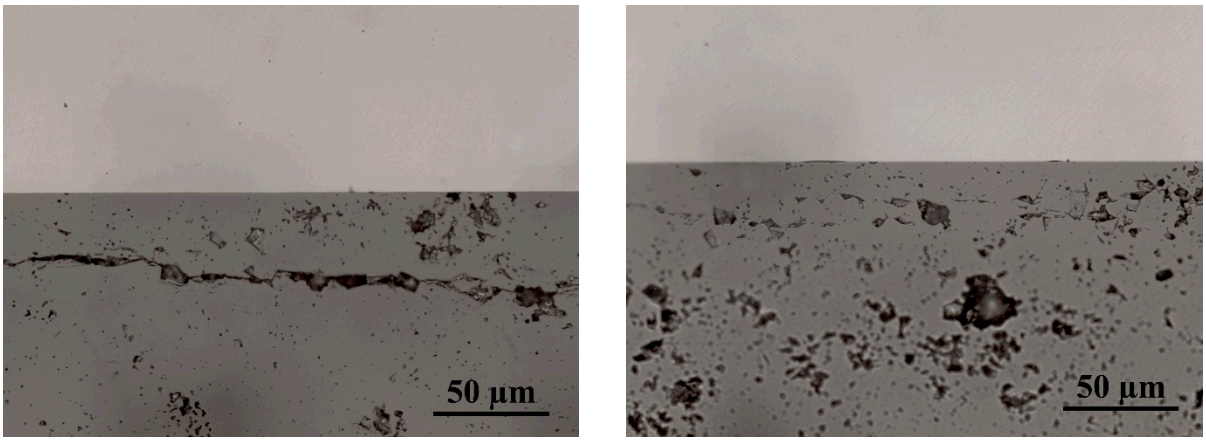

(a) **(b)**

Figure 33. High magnification image showing the UO_2-C35M interface. (a) Sample in Position 1, (b) Sample in Position 13.

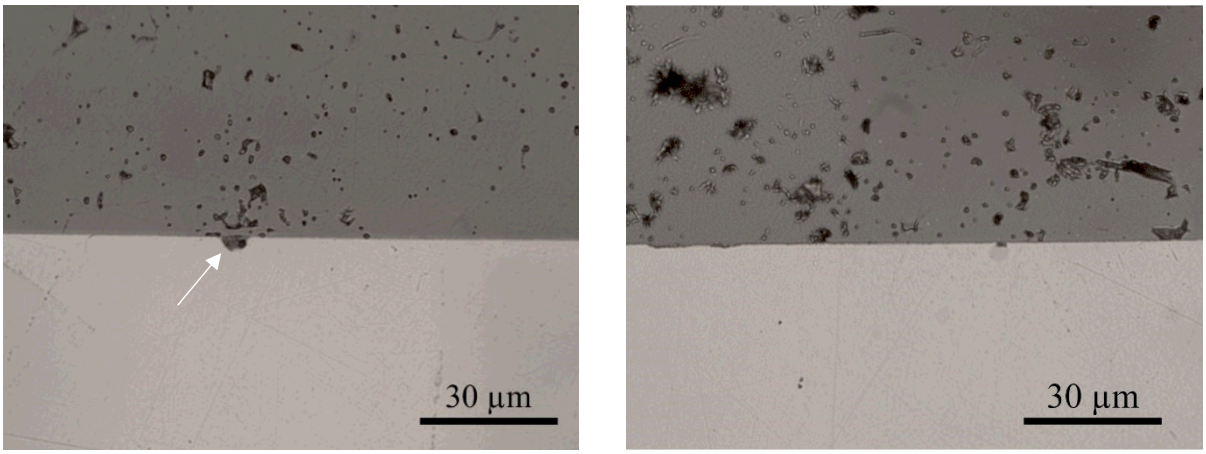

(a) **(b)**

Figure 34. High magnification image showing the UO_2-C35M interface. (a) Sample in Position 2, (b) Sample in Position 12.

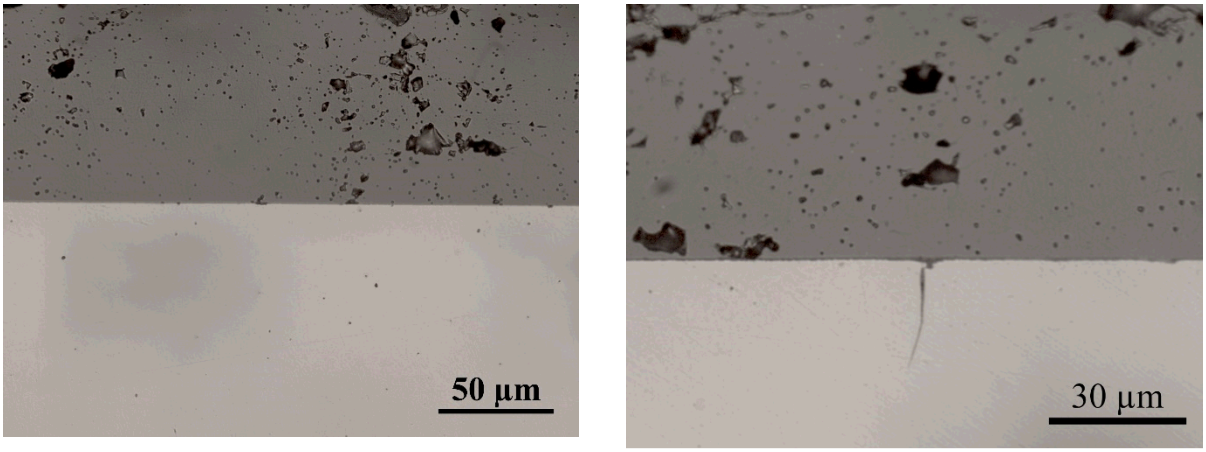

(a) **(b)**

Figure 35. High magnification image showing the UO_2-C35M interface. (a) Sample in Position 3, (b) Sample in Position 11.

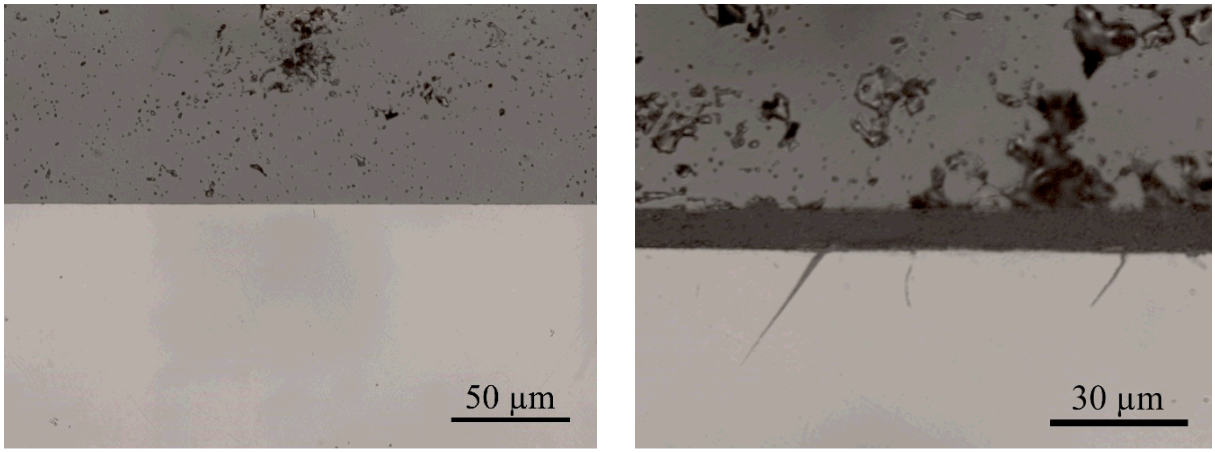

(a) **(b)**

Figure 36. (a) High magnification image showing the UO_2-C37M interface (Position 4). (b) Cracks observed along the C37M surface.

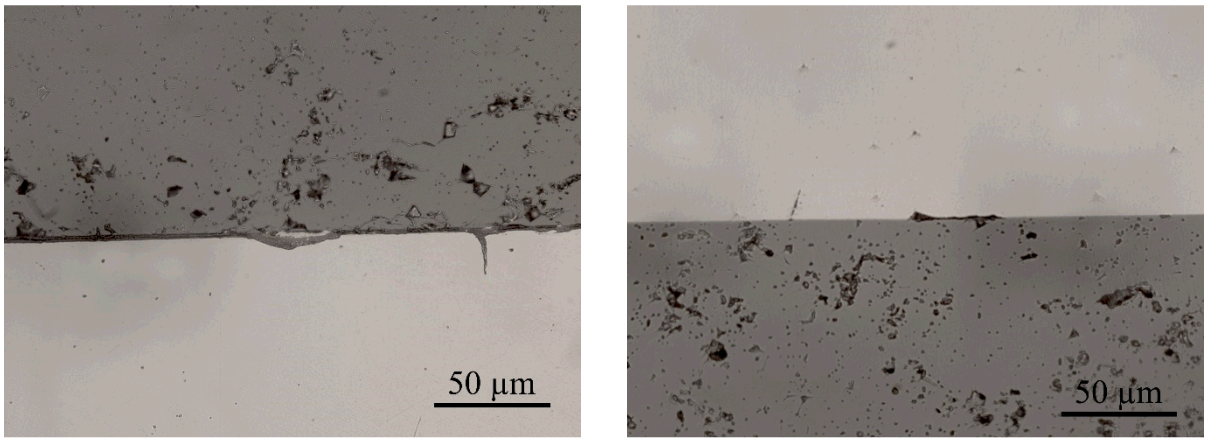

(a) **(b)**

Figure 37. (a) Localized interaction and crack on the surface of the B135Y2 small grain sample (Position 10). (b) Surface irregularity on the interface between fuel and B135Y2 large grain sample (Position 8). Both samples were pre-oxidized.

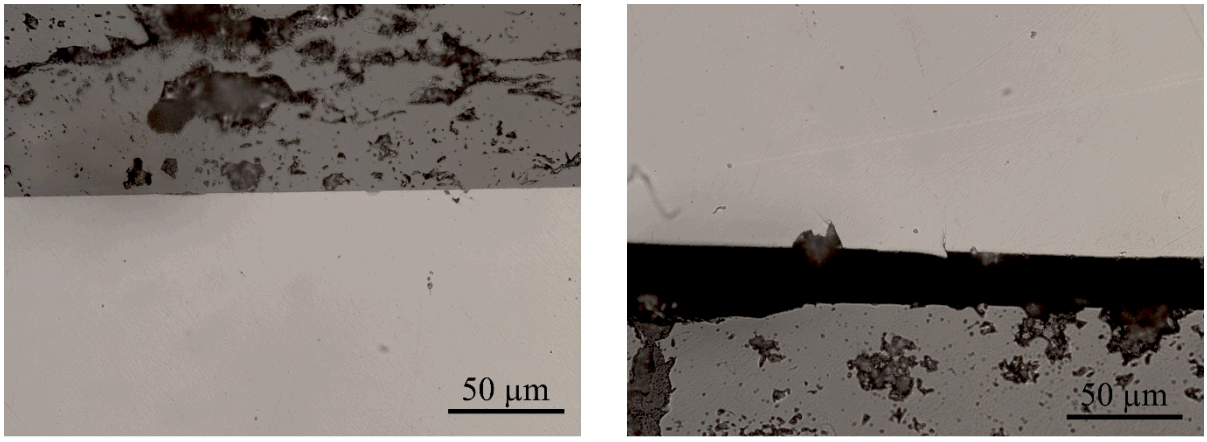

(a) **(b)**

Figure 38. (a) High magnification image of one of the unknown samples showing the appearance of the interface. (b) Localized surface defects observed outside the bonded region.

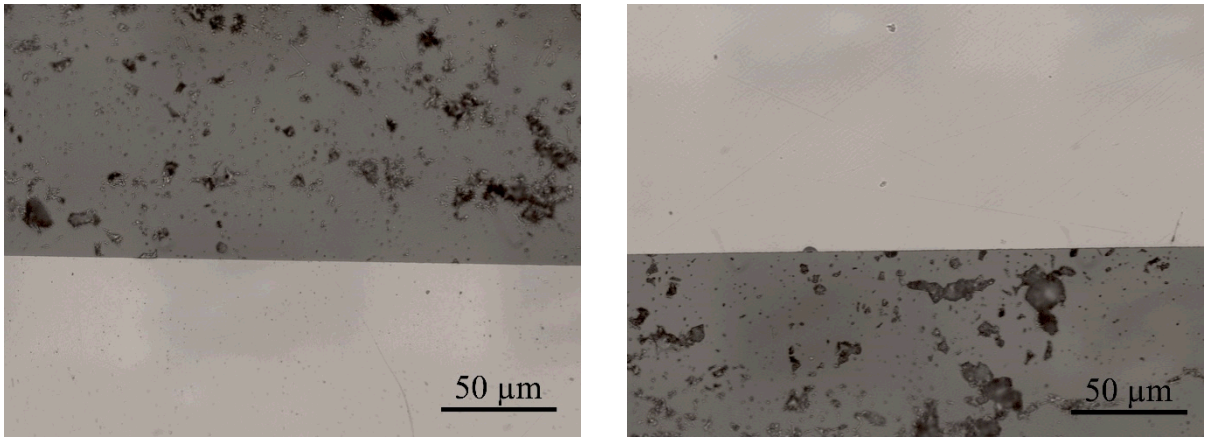

(a) **(b)**

Figure 39. (a)-(b) Appearance of the interface of the other two unknown samples, respectively.

4.2 Discussion

All the NDEs confirmed that the H-cups maintained their integrity during irradiation. The most relevant PIE data for this experiment came from optical microscopy. Examinations of the low magnification images showed similar structure among all the H-cups. Only the sample in position 13 shows partial de-cohesion of the H-cup structure (Figure 27b). Despite the reduced restrain effect of the external H-cup, contact and interaction between the fuel and the FeCrAl discs occurred during irradiation at least along the radial center of the sample, as part of the fuel remained attached to the FeCrAl discs. In all the H-cups, it was observed that the fuel is adherent to the FeCrAl discs at the radial center (i.e., close to rodlet vertical axis), while gaps could be observed towards the outer surfaces where the discs contact the restrain ring. In some of the samples, the region where the fuel is not in contact with the FeCrAl discs is marked by large cracks parallel to the FeCrAl discs (for example, see the white arrows in Figure 28a). In all the H-cups, the fuel microstructure appears similar, with porosity distributed along all the fuel disc thickness.

Figure 33 to Figure 35 show enlargements of the fuel-discs interface. Overall, no extensive interaction has occurred between the fuel and the iron-based alloys. Localized defects along the disc surfaces could be observed in the pre-oxidized samples (Figure 34 and Figure 35). Some of them appear to have circular shape (Figure 34a), resembling pitting defects. Cracks were occasionally observed. The crack length varies between a few microns and a few tens of microns; an example is reported in Figure 35b. Similar observations were made on the sample with pre-oxidized C37M discs, whose interface is reported in Figure 36. The majority of the interface appears intact (Figure 36a), but several cracks were observed, both in the region in contact with the fuel and in the outer radial regions (Figure 36b).

The interface of the other alloy B135Y was mostly pristine as well. Some areas showed a more pronounced roughness with potential onset of interaction between the fuel and the alloy (Figure 37). From the present observation, it seems that the difference in the initial grain size has no significant effect on the onset of interaction. Cracks and pitting similar to those reported for the other pre-oxidized samples were observed.

It is not known if these defects, cracks and pitting-type, were already present before irradiation or are irradiation-induced. Chemical analyses and scanning electron microscopy (SEM) are necessary to determine the composition of the sample close to these defects. More details about the composition and morphology could reveal the origin of these localized defects.

The three remaining samples are shown in Figure 38 and Figure 39. The results are consistent with the other samples described so far. Most of the fuel-cladding interface was intact. Towards the radial periphery of one of the samples, pieces of metal discs were missing, as visible in Figure 38b, but the irregularities were localized to that region.

5. ATF-45

As with the other ATF-1 capsules, PIE examinations were performed at HFEF of INL. The exam matrix is the same as for capsules ATF-06 and ATF-08. The results of these exams are summarized in the following sections.

5.1 Results from PIE

Non-destructive examinations on the capsule were completed last fiscal year, showing no defects in the capsule [18]. After removal from the capsule, the series of NDEs was conducted on the rodlet.

5.1.1 Visual inspection

Visual inspection was performed together with the ATF-1G rodlets. No unusual features were observed on the cladding surface. The dark rings at the beginning and bottom of the rodlet that can be seen in Figure 40 correspond to the locations of the end cap welds, which normally darken during irradiation.

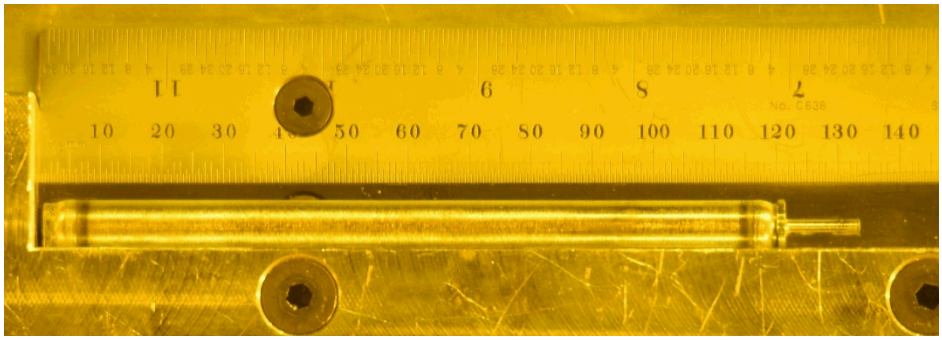

Figure 40. Visual examination of rodlet ATF-L45.

5.1.2 Neutron Radiography

Neutron radiography is reported in Figure 41. In the thermal neutron regime (left side), the enriched stack is marked by the brighter contrast due to the contribution of the induced thermal fissions from ^{235}U. In the epithermal regime, the uppermost and the lowermost pellets appear brighter instead. This is due to the increased neutron absorption by ^{235}U in the epithermal region and by the drop in the absorption by nitrogen compared to silicium in the composite depleted pellets at the top and bottom of the stack. No evidence of large cracking can be seen.

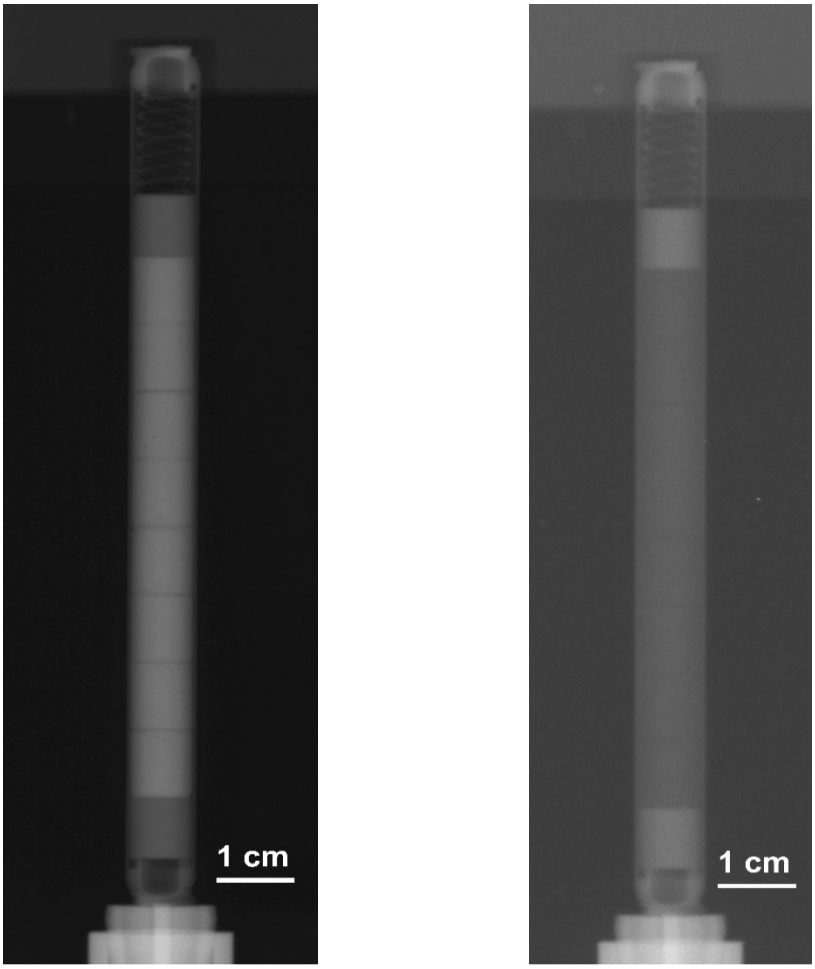

(a) **(b)**

Figure 41. (a) Thermal and (b) epithermal neutron radiographs of rodlet L45.

5.1.3 Dimensional inspection

Dimensional inspection took place at the same device used for the previous two rodlets in HFEF. The angle averaged measured diameter is reported in Figure 42.

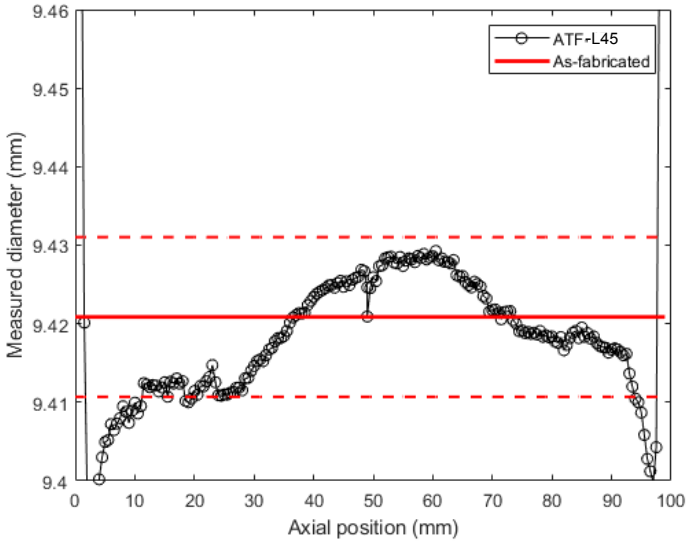

Figure 42. Angle-averaged profilometry measurements on ATF-L45.

Before dimensional inspection could be carried out, the stub at the bottom of the rodlet, which is used to sustain the rodlet during dimensional scanning, was damaged and broke off. The measurements were conducted by inserting the rodlet directly in the chuck, but, in this case, the axial alignment of the rodlet during probe scanning is less accurate. This caused the measurement drift visible in Figure 42 towards the rodlet ends. However, at mid axial position (approximately at 50 mm in Figure 42), the measurements are representative. No dimensional change could be observed when considering fabrication uncertainty.

5.1.4 Gamma Spectrometry

Gamma spectrometry is reported in Figure 43 and Figure 44. The distribution of the major fission products is not symmetric (Figure 43). As the maximum temperature of the fuel was only in the range of 800°C (see Figure 3b) and the thermal gradient along such a short rodlet is small, it is unlikely that Cs has redistributed, indicating that the asymmetry is due to higher burnup in the upper half of the rod. Both ^{106}Ru and ^{95}Zr show the same profile, corroborating this result. The content of ^{54}Mn, an activation product of ^{54}Fe from the cladding, shows a slight increase in the upper half too (Figure 44), suggesting that the fast neutron flux was higher in that part of the rodlet.

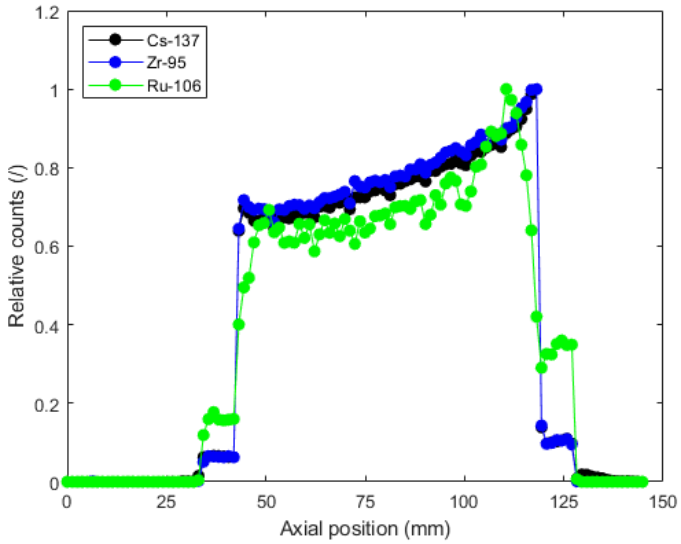

Figure 43. Axial gamma spectrometry of ATF-L45.

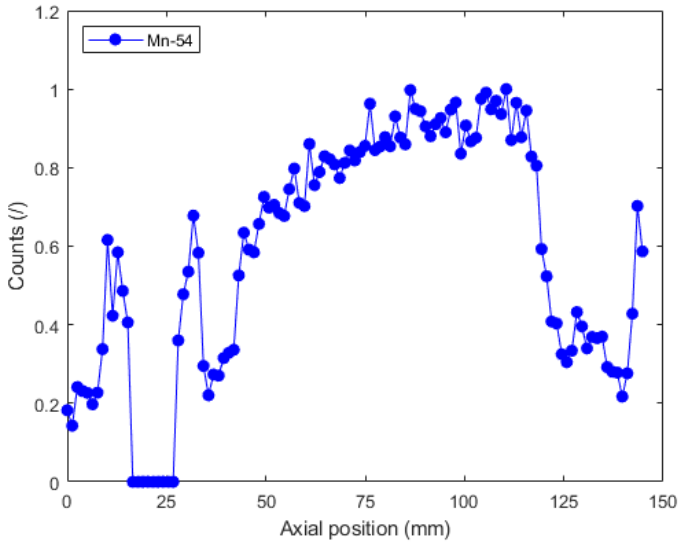

Figure 44. Axial gamma scan of the cladding activation product ^{54}Mn in ATF-L45.

The 2D gamma tomography data are shown in Figure 45. The signals from ^{144}Ce and ^{137}Cs show an increase along the pellet periphery, consistent with the expected increase in local burnup due to the self-shielding effect. Thermo-migration has occurred for the fission product ruthenium, which shows radial redistribution towards the pellet center.

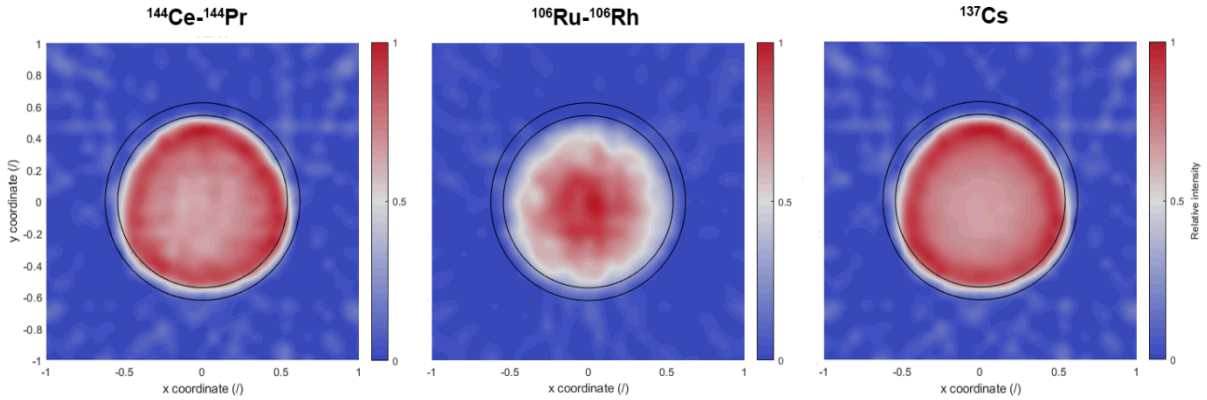

Figure 45. Gamma tomography of selected fission products for ATF-L45.

5.1.5 Fission Gas Release

The results of FGR are summarized in **Table 8**, along with calculated average fuel centerline temperature and burnup.

Table 8. Fission gas release data, calculated temperature and burnup for ATF-L45.

Rod ID	Fuel Centerline Average Temperature (°C)	Burnup (GWd/tHM)	Fission Gas Release (%)
L45	768	13.19	0.7 ±0.008

5.1.6 Optical Microscopy

Sectioning of the rodlet was performed at three different axial locations: at the top of the rodlet within the composite depleted pellet of UN-U_3Si_5 (Figure 46 and Figure 47), at 87% (Figure 48 and Figure 49), and 19% (Figure 50 and Figure 51) of the height of the active stack.

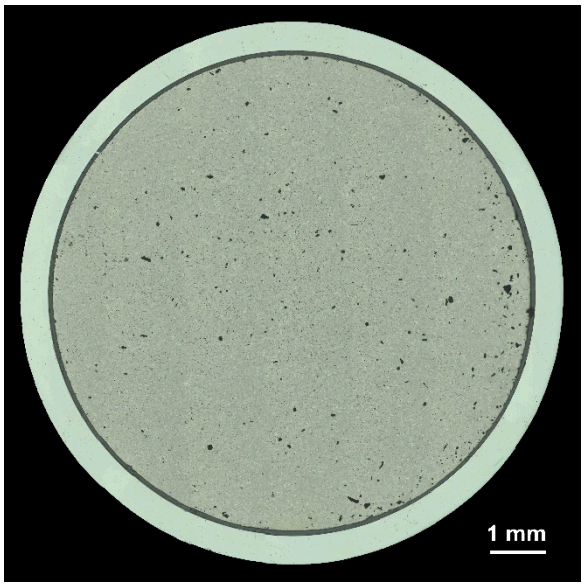

Figure 46. Radial cross section of the UN-U_3Si_5 depleted pellet above the fuel stack of L45 (50X).

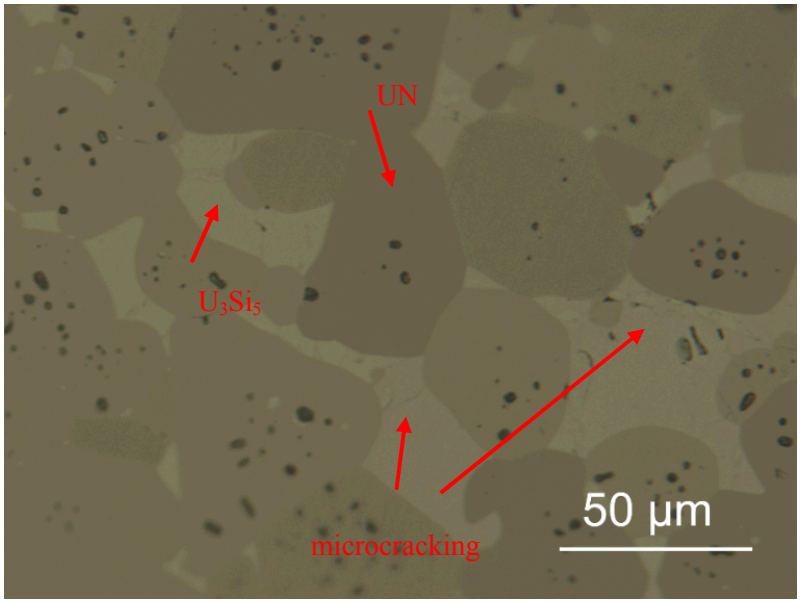

Figure 47. High magnification micrograph of the UN-U_3Si_5 structure.

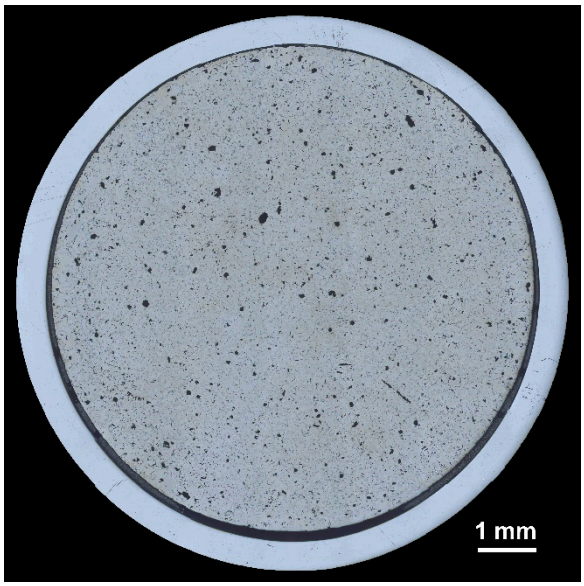

Figure 48. Radial cross section of a U_3Si_5 pellet in the upper half of the fuel stack of L45 (50X).

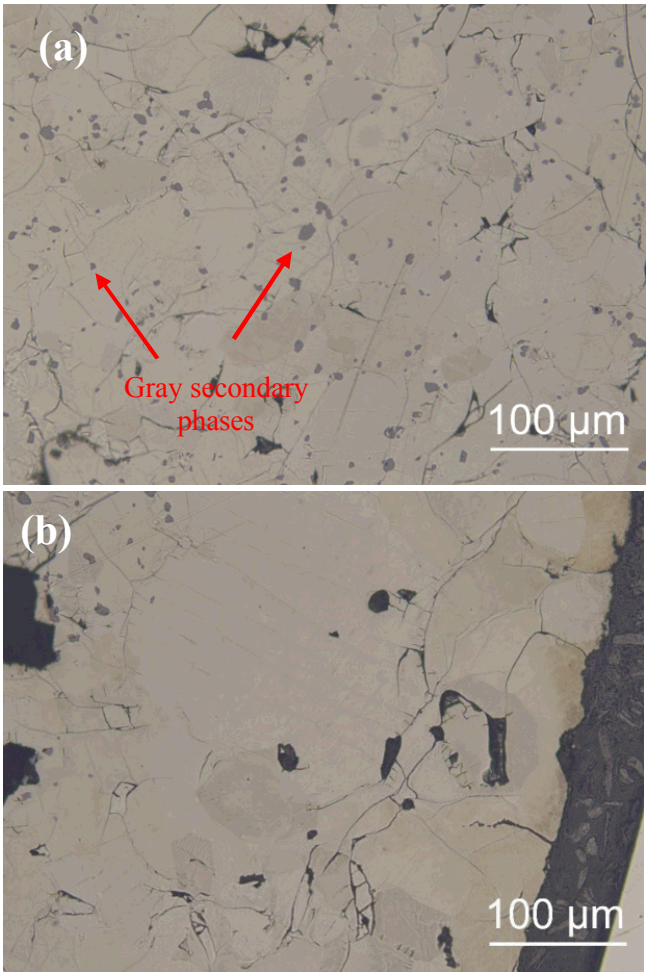

Figure 49 Overview of the U_3Si_5 microstructure from the upper-half of the fuel column (a) Pellet center, (b) Pellet periphery.

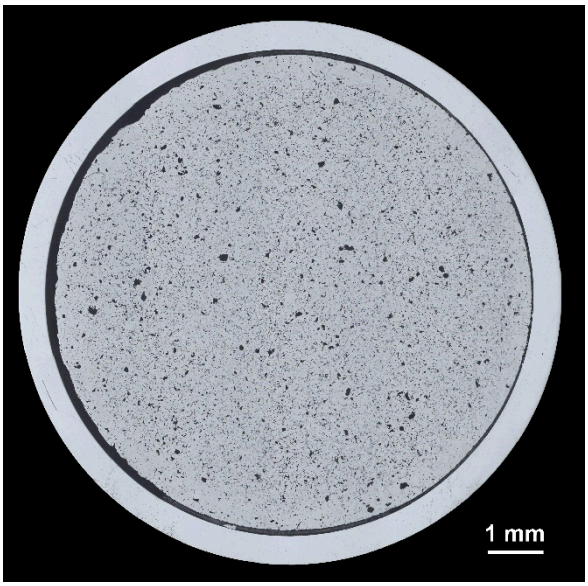

Figure 50. Radial cross section of a U_3Si_5 pellet in the lower half of the fuel stack of L45 (50X).

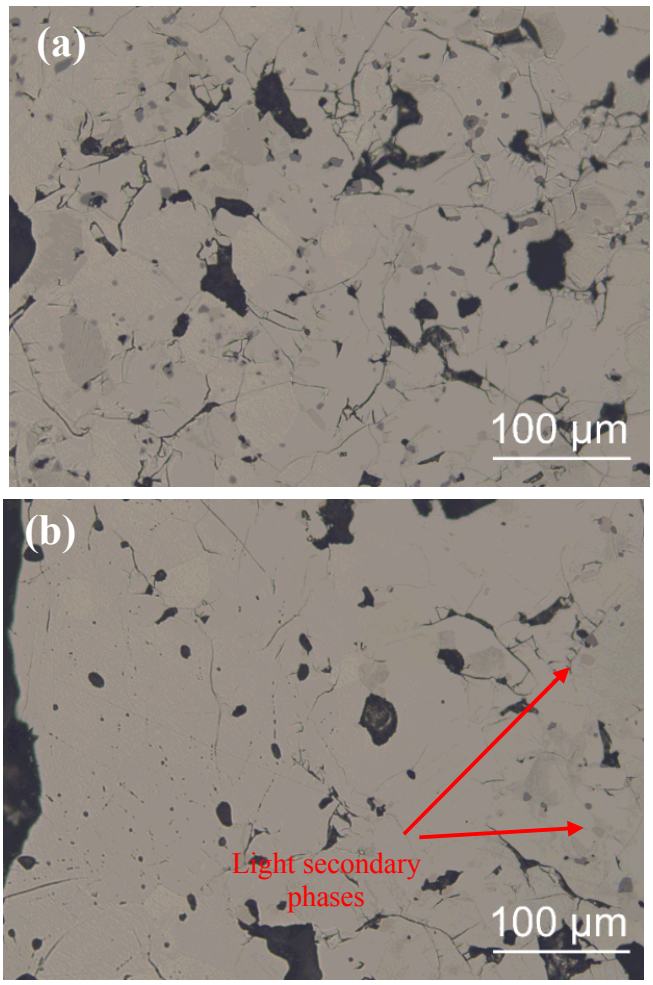

Figure 51. Overview of the U_3Si_5 microstructure from the lower-half of the fuel column (a) Pellet center, (b) Pellet periphery.

5.1.7 Cladding Microhardness

Vickers microhardness measurements were carried out in the same way as for ATF-1G. The measured Vickers microhardness across the cladding thickness is reported in Figure 52.

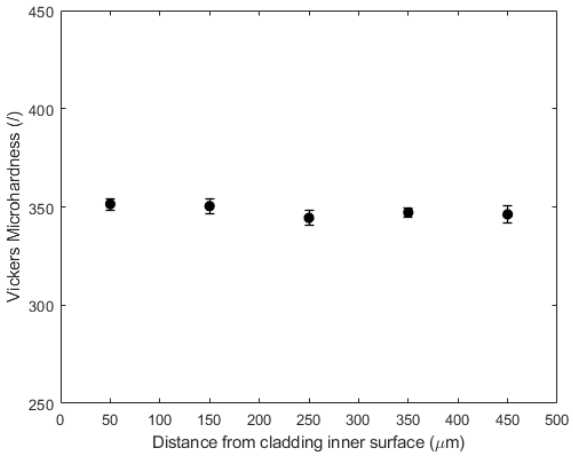

Figure 52. Microhardness profile across the cladding thickness for Kanthal AF®.

5.2 Discussion

Visual inspection and neutron radiography did not show bulging of the cladding. Dimensional analysis, not considering the bias at the top and bottom of the rodlet, did not reveal cladding hoop strain, suggesting limited contact between the fuel and the cladding. Optical microscopy confirmed the results of the non-destructive analyses as the gap was still open. The asymmetry in the gamma scan results of ^{137}Cs and other fission products can be explained by the irradiation position occupied by the rodlet in the ATR core. ATF-L45 was irradiated in the lowermost irradiation position. There is a significant axial gradient in the thermal neutron flux profile at the upper and lower edges of the ATR core. Based on neutronic calculations, the power at the top of the rodlet is ~ 120% that of the rodlet average fission power, explaining the observed gamma profile.

As can be seen from **Table 8,** the FGR remains low, because the centerline temperature stayed well below the Vitanza threshold [31] throughout all the irradiation. Overall, the microstructure of the two samples was very similar. No formation of fission gas bubbles could be observed on the surface of the two samples. Both samples showed extensive fine cracking (Figure 49 and Figure 51), which was present in the as-fabricated structure too. The micro-cracking is attributed to the phase transition occurring at 450°C [13]. Two different population of precipitates were observed: one with a dark-gray color (see for example Figure 49a), the other, far less abundant, with color similar to the matrix (shown in Figure 51b). The secondary phases were distributed homogeneously throughout the entire pellet, other than in the periphery. The outermost 350-400 μm did not contain the precipitates. This region, in both samples, also showed larger grains compared to the rest of the pellet, as can be seen from Figure 49b and Figure 51b. Both U-rich and UO_2 secondary phases have been previously reported in the as-fabricated samples [13]. In addition, pre-irradiation characterization of mock-up rodlets has identified presence of UN contamination [15]. The shape and volume fraction of the observed dark-grey phases resembles the UN phases reported for the as-fabricated microstructure. However, it is also possible that the precipitates are related to the radial redistribution of Ru. No previous study has been published in open literature regarding the behavior of ruthenium in U_3Si_5 that could provide a comparison with the observed microstructure. EDX analyses and other advanced PIE technique will be crucial to determine the nature of the precipitates observed.

A sample was cut in the depleted part of the fuel stack to observe the microstructure changes in that composite. A high magnification of the composite microstructure is shown in Figure 47. The structure resembles the as-fabricated microstructure shown in Figure 12 of Reference [15]. The silicide phase is confined to the grain boundaries of the nitride phase. The porosity is localized within the UN particles, and microcracking is visible within the silicide as it was in the pre-irradiated samples.

Vickers microhardness was constant across the cladding thickness. Vickers microhardness measurements on un-irradiated material is not available. Given the similar composition of Kanthal AF® to Kanthal APMT®, it can be expected that the microhardness for the previous will be similar to the latter. Indeed, hardness values are 230 and 250, respectively. Given this assumption, the microhardness value for Kanthal AF® can be expected to be approximately 332, which is comparable with the average value in Figure 52.

5.3 Other ATF-1 PIE

Five other ATF-1 capsules were received in April 2019 and are at varying steps in the PIE process. This section will summarize the current state of these capsules.

5.4 ATF-41 and ATF-44

Capsule visual inspection was conducted just after receipt at HFEF. The capsules appeared intact, and both neutron radiography and gamma spectrometry did not show unusual features. Thermal neutron image of the capsules in shown in Figure 53. Capsule ATF-41 appears brighter than ATF-44, as the latter had higher ^{235}U enrichment (5.27 wt% vs 2.69 wt% respectively). After performing NDEs on the capsules and assuring rodlet integrity, capsule disassembly proceeded. At the time of writing, rodlets are undergoing NDEs.

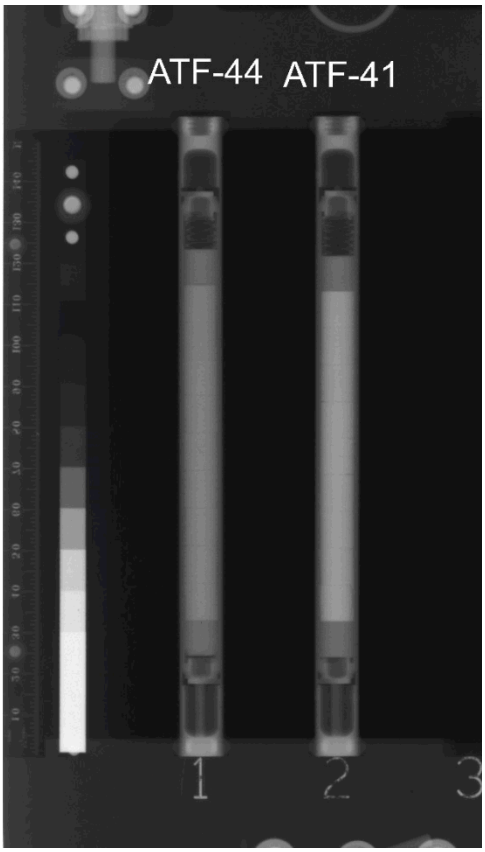

Figure 53. Thermal neutron radiography of the two capsules ATF-41 and ATF-44.

5.5 ATF-10, ATF-30 and ATF-34

Capsule visual inspections, capsule neutron radiography, and capsule gamma spectrometry have been performed on these capsules. In the thermal neutron radiograph in Figure 54, the central hole in the depleted pellets above the fuel stack which accommodate the meltwire can be seen in ATF-10. Already from the capsule exam, some cracking in the U_3Si_2 pellets is visible, both in the axial direction and parallel to the axial length. These latter cracks were attributed previously to as-fabricated defects of this first generation of pellets, but the irradiation-induced cracking is less than in UO_2 pellets [21]. The features observed in this additional capsule are consistent with the two previously analyzed. In ATF-30 and ATF-34, the meltpack space is visible between the upper depleted pellet and the active fuel stack. No cracking of the pellets is visible from the capsule exam.

At the time of writing, rodlets are undergoing NDEs.

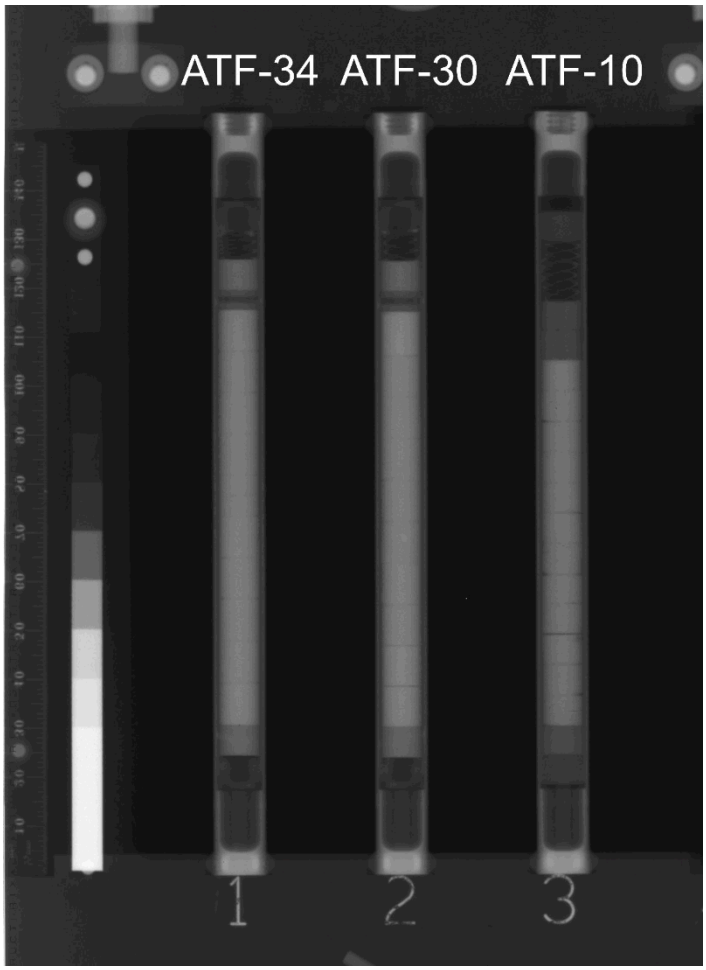

Figure 54. Thermal neutron radiography of the three capsules ATF-10, ATF-30 and ATF-34.

6. CONCLUSIONS

This report summarizes the PIE performed in 2019 on the rodlets that are currently available in HFEF from the ATF-1 irradiation tests. These irradiation tests investigated a variety of different concepts. Particularly, the report focused on five capsules received in April 2018. Both non-destructive and destructive PIE have been carried out on three rodlets focused on determining the performance of FeCrAl alloys. In addition, a U_3Si_5 pin has undergone NDEs and the microstructure characterization.

The analyses of the ATF-1G irradiations did not show anomalies in the performance of FeCrAl alloys. The claddings showed limited hoop strain; microhardness is consistent with out-of-pile data, and no wastage of the inner cladding surface could be observed. Secondary phases have accumulated on the fuel rim, but it is suspected that those are related to the radial Cs migration, consequent the high irradiation temperatures. Chemical analyses are needed to clarify this hypothesis.

Optical microscopy of the FCCI rodlet revealed no extensive interaction between UO_2 and the various FeCrAl alloys investigated. Localized defects could be seen on the FeCrAl coins surfaces and further investigations are planned to clarify whether they were fabrication defects or irradiation-induced corrosion.

PIE screening of the U_3Si_5 fuel showed that the FGR of this fuel concept remains low and comparable with what was previously reported for U_3Si_2. The fuel microstructure is comparable to the pre-irradiated material. Precipitates are visible throughout the radius of the pellets. They could be contamination phases reported from fabrication, but they could also be related to fission product precipitation. Regarding fission products, gamma tomography revealed that the gamma emitters are homogeneously distributed across the pellet radial position, with the exception of ruthenium, which migrated towards the pellet center.

ATF-1 PIE continues on several other ATF-1 capsules that are in various stages of PIE. The results of PIE will periodically be published, and further updates on the status of ATF-1 PIE will be forthcoming on the additional capsules that have begun PIE in HFEF.

7. REFERENCES

[1] J. Carmack, F. Goldner, S.M. Bragg-Sitton, L.L. Snead, Overview of the U.S. DOE Accident Tolerant Fuel Development Program, in: TopFuel 2013, 2013.

[2] F. Goldner, Overview of the accident-tolerant fuel development, in: OECD/NEA Work. Accid. Toler. Fuels LWRs, 2012: pp. 22–23.

[3] S.M. Bragg-Sitton, M. Todosow, R. Montgomery, C.R. Stanek, R. Montgomery, W.J. Carmack, Metrics for the Technical Performance Evaluation of Light Water Reactor Accident-Tolerant Fuel, Nucl. Technol. 195 (2016) 111–123.

[4] K.A. Terrani, S.J. Zinkle, L.L. Snead, Advanced oxidation-resistant iron-based alloys for LWR fuel cladding, J. Nucl. Mater. 448 (2014) 420–435. doi:https://doi.org/10.1016/j.jnucmat.2013.06.041.

[5] Nuclear Energy Agency Organisation for Economic Co-operation and Development, Nuclear Fuel Safety Criteria Technical Review, 2012.

[6] T. Cheng, J.R. Keiser, M.P. Brady, K.A. Terrani, B.A. Pint, Oxidation of fuel cladding candidate materials in steam environments at high temperature and pressure, J. Nucl. Mater. 427 (2012) 396–400. doi:https://doi.org/10.1016/j.jnucmat.2012.05.007.

[7] B.A. Pint, K.A. Terrani, M.P. Brady, T. Cheng, J.R. Keiser, High temperature oxidation of fuel cladding candidate materials in steam–hydrogen environments, J. Nucl. Mater. 440 (2013) 420–427. doi:https://doi.org/10.1016/j.jnucmat.2013.05.047.

[8] R.B. Rebak, ADVANCED STEELS FOR ACCIDENT TOLERANT FUEL CLADDING IN COMMERCIAL NUCLEAR REACTORS, in: Adv. Mater. Sci. Environ. Energy Technol. III, 2014.

[9] K.G. Field, R. Howard, M. Teague, Fabrication Control Plan for ORNL ATF Test Specimens to be Irradiated in the ATR, 2014. PLN-4655.

[10] K.G. Field, J.M. Harp, G.M. Core, K. Linton, Status of Wrought FeCrAl-UO2 Capsules Irradiated in the Advanced Test Reactor, 2017. ORNL/TM-2017/366.

[11] N.R. Brown, A. Aronson, M. Todosow, R. Brito, K.J. McClellan, Neutronic performance of uranium nitride composite fuels in a PWR, Nucl. Eng. Des. 275 (2014) 393–407. doi:https://doi.org/10.1016/j.nucengdes.2014.04.040.

[12] L.H. Ortega, B.J. Blamer, J.A. Evans, S.M. McDeavitt, Development of an accident-tolerant fuel composite from uranium mononitride (UN) and uranium sesquisilicide (U3 Si2) with increased uranium loading, J. Nucl. Mater. 471 (2016) 116–121. doi:https://doi.org/10.1016/j.jnucmat.2016.01.014.

[13] J.T. White, A.T. Nelson, D.D. Byler, D.J. Safarik, J.T. Dunwoody, K.J. McClellan, Thermophysical properties of U3Si5 to 1773K, J. Nucl. Mater. 456 (2015) 442–448. doi:https://doi.org/10.1016/j.jnucmat.2014.10.021.

[14] E. Sooby Wood, J.T. White, A.T. Nelson, Oxidation behavior of U-Si compounds in air from 25 to 1000 C, J. Nucl. Mater. 484 (2017) 245–257. doi:https://doi.org/10.1016/j.jnucmat.2016.12.016.

[15] S.C. Vogel, N.P. Borges, A.S. Losko, S.M. Mosby, S.L. Voit, J.T. White, D.D. Byler, J.T.

Dunwoody, A.T. Nelson, K.J. Mcclellan, Neutron Characterization of Encapsulated ATF-1/LANL-1 Mockup Fuel Capsules, 2017.

[16] M.I. Mirandou, R.O. González, S.F. Aricó, A.M. Fortis, Neutron Irradiation of U3Si5 and Al43Mo4U6 Compounds. First Results, Procedia Mater. Sci. 9 (2015) 404–411. doi:https://doi.org/10.1016/j.mspro.2015.05.010.

[17] J.T. White, A.W. Travis, J.T. Dunwoody, A.T. Nelson, Fabrication and thermophysical property characterization of UN/U3Si2 composite fuel forms, J. Nucl. Mater. 495 (2017) 463–474. doi:https://doi.org/10.1016/j.jnucmat.2017.08.041.

[18] J.M. Harp, F. Cappia, L. Capriotti, Postirradiation Examination of the ATF-1 Experiments - 2018 Status, United States, 2018. doi:10.2172/1484529.

[19] C.J. Murdock, B.J. Curnutt, C. Hale, Accident Tolerant Fuels Series 1 (ATF-1) Irradiation Testing FY 2018 Status Report, 2018. NL/EXT-18-51584.

[20] F. Cappia, J.M. Harp, K. McCoy, Post-irradiation examinations of UO2 composites as part of the Accident Tolerant Fuels Campaign, J. Nucl. Mater. 517 (2019) 97–105. doi:https://doi.org/10.1016/j.jnucmat.2019.01.050.

[21] F. Cappia, J.M. Harp, Postirradiation examinations of low burnup U3Si2 fuel for light water reactor applications, J. Nucl. Mater. 518 (2019) 62–79. doi:https://doi.org/10.1016/j.jnucmat.2019.02.047.

[22] K. Linton, Y. Yan, Z. Burns, K. Terrani, Hot Cell Installation and Demonstration of the Severe Accident Test Station, 2017.

[23] A.E. Craft, D.M. Wachs, M.A. Okuniewski, D.L. Chichester, W.J. Williams, G.C. Papaioannou, A.T. Smolinski, Neutron radiography of irradiated nuclear fuel at Idaho National Laboratory, Phys. Procedia. 69 (2015) 483–490.

[24] J.M. Harp, P.A. Demkowicz, Investigation of the Feasibility of Utilizing Gamma Emission Computed Tomography in Evaluating Fission Product Migration in Irradiated TRISO Fuel Experiments, in: Int. Top. Meet. High Temp. React. Technol. (HTR 2014), WeiHai, China, 2014.

[25] R.S. Forsyth, W.H. Blackadder, N. Ronqvist, Burn-Up Determination by High Resolution Gamma Spectrometry Fission Product Migration Studies, Stockholm, 1967.

[26] Standard method for Vickers indentation hardness of advanced ceramics, (1999).

[27] R.B. Rebak, Ferritic Alloys as Accident Tolerant Fuel Cladding Material for Light Water Reactors, 2014.

[28] P. Medvedev, Private communication, (2019).

[29] C.T. Walker, C. Bagger, M. Mogensen, Observations on the release of cesium from UO2 fuel, J. Nucl. Mater. 240 (1996) 32–42. doi:https://doi.org/10.1016/S0022-3115(96)00477-1.

[30] H. Kleykamp, The chemical state of LWR high-power rods under irradiation, J. Nucl. Mater. 84 (1979) 109–117. doi:https://doi.org/10.1016/0022-3115(79)90154-5.

[31] C. Vitanza, E. Kolstad, U. Graziani, Fission gas release from UO2 pellet fuel at high burn-up, in: ANS Top. Meet. Light Water React. Fuel Perform., n.d.: pp. 361–366.